gels

MDPI

*Review*

# Structural Design and Cyclic Reliability of Conductive Hydrogel Strain Sensors

**Jiajia Deng and Sheng Hu ***

School of Chemical and Environmental Engineering, Hubei Minzu University, Enshi 445000, China; jiajiadeng04@outlook.com
* Correspondence: 2009002@hbmzu.edu.cn

**Abstract**

Conductive hydrogels combine compliance, stretchability, and electrical responsiveness, enabling deformation sensing through resistance or capacitance changes and providing a material basis for wearable motion monitoring. However, toughness, low hysteresis within a single cycle, and repeatable output over prolonged cycling describe distinct properties; none alone establishes whether a sensor retains its original calibration during sustained use. Understanding this distinction requires examining how differences in the extent and timescale of recovery in load-bearing structures, conductive pathways, and interfacial contacts produce asynchronous changes in mechanical state, signal baseline, response amplitude, and loading–unloading trajectories. This review examines structural design and cyclic reliability in conductive hydrogel strain sensors, analyzing how reversible connections, interchain constraints, and interphase coupling affect mechanical dissipation and conductive-pathway rearrangement, and how device interfaces influence deformation transfer and electrical readout. It further evaluates the applicability and performance limits of structural strategies by considering crack resistance–cyclic dissipation trade-offs and the relationships between recovery time, loading schedule, strain amplitude, loading rate, hydration state, and readout conditions. Cyclic reliability should therefore be evaluated through calibration retention and strain measurement error under specified operating conditions, linking material recovery to specific measurement tasks and guiding the coordinated selection of material structures, device interfaces, and operating conditions.

**Keywords:** conductive hydrogels; strain sensing; network recovery; signal hysteresis; cyclic reliability

Check for updates

Academic Editor: Marieta Constantin

Received: 22 October 2026
Revised: 13 November 2026
Accepted: 16 November 2026
Published: 18 November 2026

**Copyright:** © 2026 by the authors. Licensee MDPI, Basel, Switzerland. This article is an open access article distributed under the terms and conditions of the Creative Commons Attribution (CC BY) license.

## 1. Introduction

Joint flexion and extension, as well as soft robot motion, repeatedly stretch and retract strain sensors. Sensors used in these settings must deform with a compliant interface while continuously converting deformation into readable electrical signals. Conductive hydrogels comprise hydrated polymer networks and conductive components, such as ions, conducting polymers, or conductive fillers. Their compliance, adaptability to deformation, and electrical responsiveness provide a material basis for conformal strain sensing [1–3]. Studies ranging from dynamic deformation detection with nanoparticle-reinforced hydrogels to cyclic capacitive responses in layered hydrogel fibers have demonstrated their ability to sense repeated motion [4,5]. Practical measurement further requires a reproducible correspondence between a given strain and its signal across cycles and periods of use, while meeting measurement requirements as motion amplitude and speed change. How the

structural state of a material affects sustained strain measurement is therefore a key question connecting conductive hydrogel design with practical applications.

This question involves three related but noninterchangeable aspects: network recovery, signal hysteresis, and cyclic reliability. Network recovery concerns the extent to which load-bearing structures and their mechanical responses recover after unloading. Signal hysteresis describes the difference between electrical outputs at the same strain during loading and unloading. Cyclic reliability concerns whether a device maintains the required measurement capability under specified conditions throughout a period of use [6]. These properties do not necessarily change together. In physically crosslinked double-network gels, peak stress, modulus, and dissipated energy recover to different extents after the same waiting period, showing that recovery depends on the physical quantity being observed [7]. Regarding electrical response, conducting polymer gels with interlocked microphases can achieve low hysteresis and repeatable strain responses [8]. Repeatable output does not, however, imply coincident loading and unloading trajectories: encapsulated poly(vinyl alcohol) (PVA) gels can exhibit repeatable output alongside loading–unloading hysteresis [9]. Waveform repeatability also differs from baseline stability; for example, antiswelling gels can undergo overall signal drift while their waveform and amplitude remain relatively stable [10]. Assessing cyclic reliability therefore requires connecting recovery of specific physical quantities with actual measurement capability and examining whether the original calibration remains valid during sustained use.

Structural designs addressing these issues improve behavior under repeated deformation by modifying load-bearing networks, the organization of conductive components, and device interfaces. Within load-bearing networks, movable crosslinks in polyrotaxane structures redistribute chain tension, providing a structural route to maintaining subsequent load bearing. Adjusting nanoparticle connection topology and swelling state can reduce cyclic mechanical dissipation by alleviating transient chain constraints [4,11]. To coordinate load bearing and conduction, microphase interlocking between a conducting phase and a mechanical network helps reduce interphase sliding and separation. Layered hydrogel fibers arrange distinct functional layers to coordinate load bearing, conduction, and interfacial capacitive response [5,8]. At the device level, studies of elastomer-encapsulated hydrogel sensors demonstrate cyclic output from fully assembled devices [9]. These designs act on load distribution, conductive-phase connectivity, and device protection, respectively, and thus improve different structural processes.

Whether structural improvements translate into sustained measurement capability also depends on how recovery processes match the actual loading schedule. Reformation of reversible connections, chain relaxation, and adjustment of conductive pathways occur on different timescales. The interval between successive loading events determines how far these processes can proceed before the next deformation begins. Thus, even at the same strain amplitude, changing the loading rate or waiting time between cycles may alter hysteresis loops and subsequent output. A state stabilized by precycling also differs from the state at first use [6]. In intermittent measurement with pauses, waiting after unloading may allow time for network rebuilding. Rapid continuous measurement relies more strongly on timely coordination of load-bearing structures and conductive states during successive deformations. Hydration state and contact conditions also affect the responses of internal networks, transport pathways, and device interfaces [2,7]. Evaluating a structural strategy requires identifying the recovery or transport process it improves and the strain–signal relationship it can maintain under the actual loading schedule.

Existing reviews provide an important basis for understanding the cyclic performance of conductive hydrogels. Reviews of low-hysteresis gels and tough hydrogels discuss network structure, cyclic dissipation, and the relationship between toughness and hysteresis,

whereas reviews of mechanically robust conductive hydrogel sensors connect network design with mechanical properties, sensing mechanisms, and applications [12–14]. Reviews of wearable sensing further distinguish mechanical from electrical hysteresis and discuss how drift, loading history, environmental conditions, and test reporting affect reliability assessment. Reviews of conductive PVA hydrogels also address standardized evaluation, repeatability, and performance comparison [6,15]. Building on this understanding, it remains necessary to connect the specific structural features altered by each design, their recovery processes, and the associated timescales with actual output changes in strain sensors. Comparisons among studies should distinguish resistive and capacitive readout mechanisms and consider strain ranges and recovery conditions. This allows different structural causes underlying similar signal behavior to be identified and clarifies whether the reported results support the same design conclusions.

This review focuses on conductive hydrogels with water as the predominant liquid phase for resistive or capacitive strain measurement. It examines network recovery during repeated deformation and its effects on signal hysteresis and cyclic reliability. Centered on the correspondence between recovery of load-bearing networks and recovery of electrical response, the review compares how structural strategies affect hysteresis, signal drift, and calibration retention, and analyzes their applicability under different operating conditions. For structural damage, it distinguishes the cyclic endpoints associated with loss of material load-bearing capacity and loss of measurement performance, avoiding the treatment of material failure, signal changes, and device measurement failure as a single event. Related systems containing organic cosolvents are considered only as boundary comparisons, with attention to liquid-phase composition and its effects on network and transport processes [2]. By connecting structural changes, recovery processes, and measurement performance, this review seeks to clarify when different designs can maintain the required strain–signal relationship. This provides a basis for selecting material and device structures for continuous or intermittent operation and for verifying cyclic measurement capability.

## 2. Structural and Mechanical Foundations of Conductive Hydrogels

### *2.1. Composition and Network Structure*

Conductive hydrogels consist of a hydrated polymer network and components that participate in charge transport. Connections and constraints between polymer chains form a continuous network that maintains the overall shape while accommodating large amounts of water. Water participates in chain hydration, swelling, and molecular motion and provides a liquid environment for mobile ions. Charge-transport components mainly include dissolved electrolytes, conducting polymers, and dispersed conductive fillers; some also contribute to network construction. For example, polysaccharides with ionizable groups can participate in gel formation while influencing ion distribution and local interactions [1,16]. In gels containing organic cosolvents such as glycerol, water and the organic solvent jointly constitute the liquid phase during testing. Solvents used during preparation may instead be exchanged during subsequent processing and no longer remain in the final tested system [2]. In terms of chain composition, a homopolymer is formed from one monomer, whereas a copolymer is formed from two or more monomers. Copolymer chains may have block, alternating, or statistical sequences, with different monomer units covalently connected along the same chain. Chain chemistry and interchain connectivity describe distinct aspects of hydrogel structure.

In hydrogel design, a polyacrylamide backbone can provide a hydrated load-bearing framework while conducting components are introduced separately [17]. Copolymerization instead places different functional units along the same chain. In poly(acrylamide-co-maleic acid) gels, maleic-acid units provide sites for calcium coordination, coupling reversible

network connections with ionic conduction [18]. This compositional choice is distinct from combining separately formed polymers or networks.

Connections between polymer chains maintain network integrity, restrict relative chain motion, and influence load transfer during deformation. Under given test conditions, stable covalent crosslinks can provide persistent connections, whereas physical interactions such as ionic associations and hydrogen bonds may dissociate under force and reform under suitable conditions. A single physical network can contain connections of different strengths and lifetimes: more persistent connections maintain the overall structure, while readily rearranged connections allow local chain adjustment [19]. Entanglements between long chains provide another type of constraint. Interpenetrating chains cannot freely pass through one another, so relative chain motion is restricted even without chemical bonds at entanglement sites [20]. In some mechanically interlocked networks, crosslinks can slide along threaded polymer chains, changing the effective strand length between adjacent crosslinks and redistributing load [11]. The effects of these connections and constraints also depend on observation time. Molecular connectivity affects network relaxation, and reversible connections require time to reorganize [21]. Whether structural adjustment can be completed also depends on the specified loading time.

Beyond interchain connectivity, overall structure can be described by the number of networks and their relationships. A single network provides the main constraints through one continuous crosslinked structure, whereas a multiple-network material contains two or more networks. A double network emphasizes the combination and joint action of two networks: classical double-network gels coordinate load bearing and energy absorption through networks with different properties. Ionic–covalent double networks use reorganizable ionic connections and a relatively stable covalent framework for local structural adjustment and overall shape retention, respectively [22,23]. Network interpenetration provides another structural description. A semi-interpenetrating network consists of a crosslinked network penetrated by uncrosslinked polymer chains, whereas an interpenetrating network consists of two separately crosslinked, interpenetrating networks without covalent connections between them. The key distinction is whether the chains penetrating another network themselves form a crosslinked network. Chain chemistry does not determine this interpenetration relationship. Chain length, polymer concentration, and crosslinking conditions also affect interchain entanglement, which can coexist with movable connections [24–26]. Chain composition, network number, interpenetration, and interchain constraints therefore describe different structural levels and can jointly characterize the same hydrogel [27]. Figure 1a separates network number from interpenetration: these describe complementary structural features rather than mutually exclusive gel categories.

Alongside connectivity and interpenetration, the spatial distribution of network components affects structure and load bearing. Phase separation may produce polymer-rich and relatively water-rich regions. Crosslink density and gelation conditions can restrict the further growth of these regions, retaining heterogeneity at particular length scales [28,29]. Crystallization and orientation produce different forms of spatial organization. Crystallization forms ordered crystalline regions, whereas orientation denotes preferential alignment of polymer chains or other structural units along a direction. Microcrystals, fibers, and amorphous regions can jointly form hierarchical structures [30]. Hydration state and mechanical deformation further change the actual network structure. Dehydration increases polymer volume fraction and alters interchain distances and interactions. Its mechanical effects may involve both entanglements and other structural changes and cannot be attributed entirely to increased entanglement [31]. Chain orientation and crystalline regions may also evolve during stretching [30]. Some slide-ring gels undergo strain-induced crystallization during extension, and the resulting crystals disappear during retraction [32]. The actual network

state of a conductive hydrogel therefore depends on both initial preparation conditions and subsequent hydration and deformation histories.

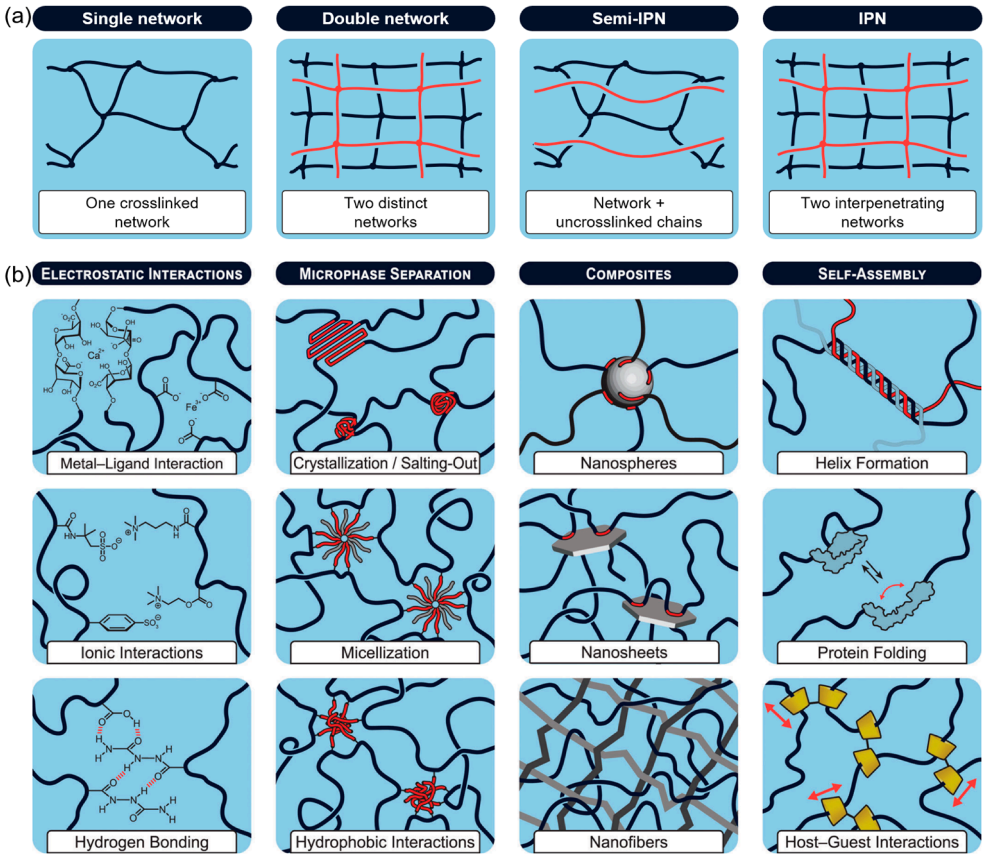



**Figure 1.** (**a**) Schematic illustration of hydrogel network architectures. (**b**) An overview of energy dissipation modes each represented by a specific molecular interactions/architectures, which have served the fabrication of tough hydrogels. Individual modes of energy dissipation are categorized according to electrostatic interactions, microphase separation, composites, or self-assembly [33].

### *2.2. Deformation and Energy Dissipation*

Stretching changes polymer-chain conformation and orientation, while network connections and constraints translate these local changes into macroscopic load-bearing responses. For initial gauge length, $L_0$, initial cross-sectional area, $A_0$, and current gauge length, $L$, engineering strain is $\varepsilon = \frac{L-L_0}{L_0}$, stretch ratio is $\lambda = \frac{L}{L_0} = 1 + \varepsilon$, and nominal stress is $\sigma = \frac{F}{A_0}$, where $F$ is the tensile force. Shear deformation is described by shear strain $\gamma$. The slope over a specified interval of the stress–strain curve characterizes the tensile modulus, the maximum nominal stress gives the tensile strength in that test, and elongation at break describes deformation at failure [33]. These quantities, respectively, indicate resistance to deformation, stress-bearing capacity [34]. The slope of a gel's curve may vary substantially with strain. Modulus comparisons therefore require a specified fitting interval and consistent reference dimensions, loading rate, and hydration state. A complete tensile curve also reveals responses over different strain intervals, providing information about deformation that a single maximum stress or elongation at break cannot capture [35]. Macroscopic photographs of the $H_{37}C_3K_6$ hydrogel reported by Ji et al. illustrate deformation and load bearing through stretching from straight and curled configurations and supporting a 500 g weight (Figure 2a) [36].

Integrating loading and unloading curves quantifies mechanical work during deformation. On a nominal stress–engineering strain curve, the area under the loading curve

gives the input work density $W_{in}$, and the area under the unloading curve, taken as positive, gives the returned work density $W_{out}$. Both are normalized by the initial specimen volume. Specifically, $W_{in} = \int_0^{\varepsilon_{max}} \sigma_{load}\, d\varepsilon$ and $W_{out} = \int_0^{\varepsilon_{max}} \sigma_{unload}\, d\varepsilon$, where the upper limit is the maximum engineering strain in the cycle and $\sigma$ is taken from the corresponding loading or unloading branch. Using kPa for stress gives work densities in kJ $m^{-3}$. The areas representing input, returned, and unreturned work are illustrated in Figure 2b for an idealized closed loading–unloading cycle. Their difference, $W_{in} - W_{out}$, is the mechanical work density not returned through unloading during that cycle [37]. Noncoincident loading and unloading paths produce mechanical hysteresis, which can be characterized by the loop area or its fraction of the loading work [33]. This work-loss fraction compares loading and unloading within one cycle. A recovery fraction measured after rest instead compares the same energy term across different cycles and requires a specified reference cycle. In initial cycles involving structural changes, unreturned work also reflects changes in material state; the loop alone cannot assign all of this work to a single molecular dissipation mechanism [33]. Integrated energy must also be interpreted according to its normalization: integrating the tensile curve of an unnotched specimen to failure gives input work per initial volume, in $J/m^3$, whereas energy per area associated with crack growth is expressed in $J/m^2$. These quantities differ in specimen conditions, normalization, and physical meaning.

Incomplete return of mechanical work during unloading is associated with internal network rearrangement. Figure 1b groups common dissipative structures in tough hydrogels into electrostatic interactions, microphase separation, composites, and self-assembly. Metal coordination, ionic associations, and hydrogen bonds constrain chains through molecular connections, while crystalline regions, micelles, and hydrophobic aggregates provide local constraints. Nanospheres, nanosheets, and nanofibers introduce polymer–filler contacts; helices, folded proteins, and host–guest units have conformations or binding states that can change. Under force, these connections and structures dissociate, slide, or change conformation, directing mechanical work into internal rearrangement [33]. Reversible connections can dissociate progressively and release previously constrained chains while a more stable framework continues to transfer load, preventing local connection changes from immediately causing overall fracture. Ionic–covalent networks and networks containing strong and weak ionic associations illustrate this division between load bearing and local rearrangement [19,23]. Relative chain sliding and relaxation of transient entanglements can also contribute to dissipation; combinations of different constraints can therefore produce different loading–unloading paths [4,38]. Some changes reverse during unloading or after rest, while others involve irreversible chain scission or damage. Mechanical loops reflect the combined macroscopic response to these processes; recovery tests and structural observations help distinguish their contributions.

Connection reorganization and chain motion take time, so the apparent stiffness and mechanical hysteresis of gels may vary with loading rate. When the loading time is shorter than the time required for a structural rearrangement, the relevant structures act as more persistent constraints during that test; their relaxation becomes apparent over longer observation times. Stress relaxation tests record stress over time at fixed strain, whereas creep tests record strain over time at fixed stress, probing time dependence under different control conditions [39]. Studies of transient entanglement networks and comparative studies varying interchain constraints show that network structure can affect the timescale of stress relaxation [21,38]. Rapid continuous cycling and loading with rest periods between cycles allow different amounts of time for network rearrangement and may therefore produce different mechanical responses.

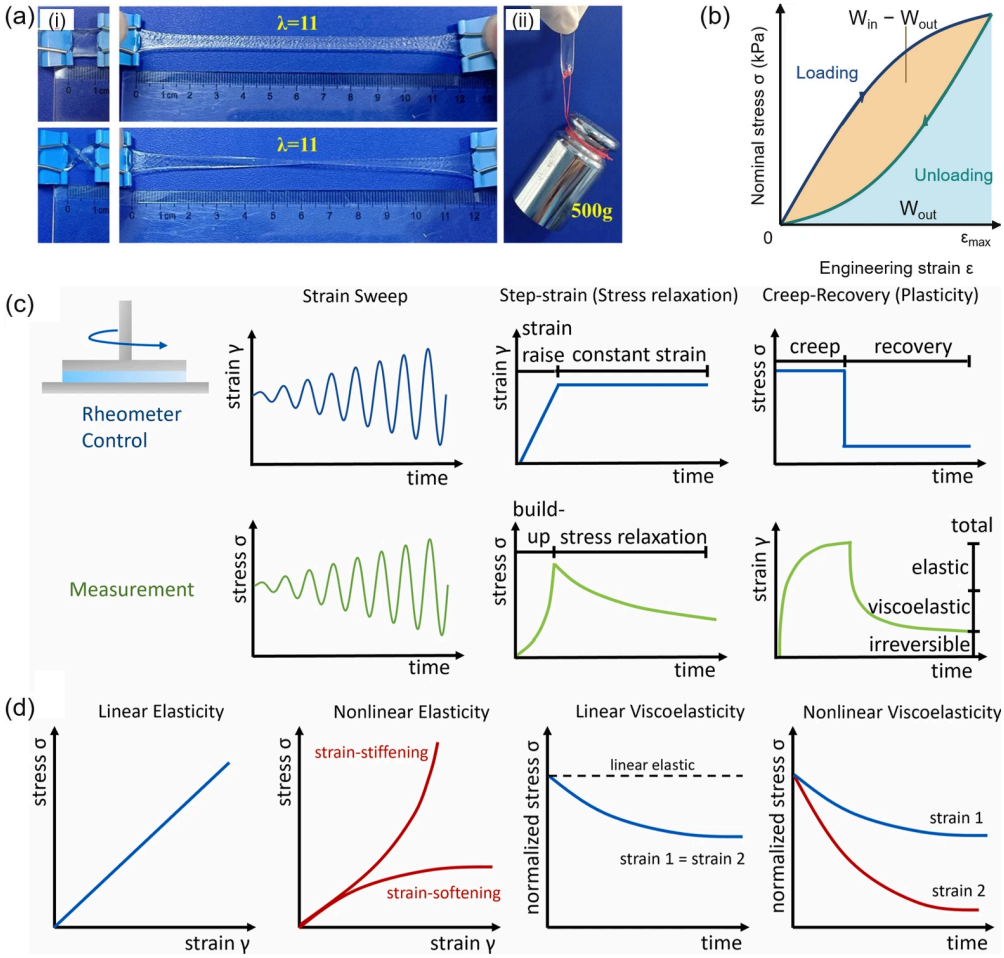



**Figure 2.** (**a**) Photographs of $H_{37}C_3K_6$ hydrogel showing (**i**) stretching and curly stretching and (**ii**) holding a 500 g weight [36]. (**b**) Input and recovered work densities during a loading–unloading cycle. (**c**) Rheometer control and measured parameters for strain sweeps to determine stress–strain response, step-strains to determine viscoelastic stress relaxation, and creep-recovery experiments to determine viscoplasticity of materials. (**d**) Schematic overview of linear and nonlinear elasticity as well as linear viscoelasticity showing the same stress relaxation at two different strains or the same strain at two different points in time and nonlinear viscoelasticity showing strain-dependent stress relaxation [39].

Water migration introduces time dependence alongside internal network rearrangement. Network deformation, liquid pressure, and relative motion between the network and solvent are coupled, so swelling involves both liquid uptake and network extension. Classical studies of gel swelling show that network–solvent coupling and specimen dimensions influence this process [40]. During mechanical testing, drainage, water exchange with the surroundings, and test duration all affect the observed response. Water loss in an open environment alters the material state for subsequent tests, while mixed-solvent composition can change water retention and environmental stability [2]. Swelling time describes the rate of liquid exchange and network expansion; recovery time after unloading describes the return process following load removal. Their driving conditions differ, so these times cannot be directly equated.

A preparation-stage example illustrates why the mass reference matters. Zhu et al. reported swelling multiples of 3.1 and 40.3 for the HEDN1st-0.2 and HEDN1st-2.0 first networks, respectively, after 24 h in a second-network precursor containing 4 M acrylamide [35]. Here, $S = m_2/m_1$ compares the swollen mass with the initial mass of the already formed

first-network gel. These values describe precursor-network expansion during fabrication, rather than dry-mass swelling or long-term uptake of a finished sensor.

### 2.3. Unloading and Cyclic Recovery

After unloading, a stretched network retracts toward its original shape, while internal connections may rebuild. As the external force decreases, the elastic network that remains connected drives chains toward more relaxed conformations. Chains and local network regions displaced during loading continue to adjust, and dissociated reversible connections may reform. In ionic–covalent networks, the shape-maintaining framework and reforming ionic connections contribute separately to recovery. Networks with associations of different strengths can also reestablish local constraints over time [19,23]. In specific slide-ring gels exhibiting strain-induced crystallization, retraction during unloading is accompanied by melting of the crystals formed during stretching [32]. Elastic retraction, connection rebuilding, and these specific structural changes may occur concurrently without finishing at the same time. Shape return and internal structural recovery must therefore be observed separately, and their rates and extents depend on loading amplitude and waiting time after unloading.

The temporal features of these processes can be observed by controlling mechanical input and recording the corresponding response. Using rheological tests as examples, Figure 2c relates controlled and measured quantities, with $\gamma$ denoting shear strain. Strain sweeps progressively vary oscillatory shear amplitude and measure the stress response. Applying a step strain and then holding strain constant reveals stress relaxation; applying a constant stress and subsequently unloading reveals creep and subsequent strain recovery. Immediate rebound and delayed recovery after unloading, respectively, reflect faster elastic return and slower structural motion. Figure 2d further illustrates the effects of deformation amplitude and time. Linear elasticity gives an approximately constant stress–strain slope, whereas nonlinear elasticity may exhibit strain hardening or softening. Within the linear viscoelastic regime, normalized stress relaxation curves at different step strains can overlap; this does not imply equal absolute stresses. In nonlinear viscoelasticity, the shape of the relaxation curve may change with strain amplitude. Loading amplitude determines the deformation regime, while observation time determines how much delayed recovery can be recorded. Residual deformation measured over a finite period alone is insufficient to establish permanent plasticity [39].

Recovery must be described using specific mechanical quantities. Residual strain after unloading indicates shape recovery. Under identical reloading conditions, the slope over a specified strain interval, peak stress, and loop area, respectively, describe recovery of tensile modulus, load-bearing capacity, and dissipative behavior. These quantities may recover to different extents during the same rest period, so recovery fractions must be assigned to the corresponding physical quantities [7,41]. For shape recovery, residual strain is referenced to the initial gauge length. Dividing it by the maximum strain of that cycle instead gives residual deformation relative to maximum deformation; the normalization differs [42]. Dissipation recovery compares the retested loop area with that of a specified reference cycle. It differs from the fraction of loading work not returned during unloading within one cycle [41]. Rheological tests use storage and loss moduli to probe elastic and viscous responses, respectively. Tracking these quantities after returning from a large-amplitude shear disturbance to small-amplitude shear reveals viscoelastic recovery, but uses different controls and observables from reloading a tensile specimen after unloading [43]. Continuous cycling tests whether responses can be maintained within the operating cycle; retesting after a specified rest period tests whether additional waiting further restores

structural and mechanical states. The recovered quantity, reference state, waiting time, and denominator used to calculate recovery jointly define the reported extent of recovery.

The reference state itself depends on loading history. Precycling and mechanical training can reorganize a network, and prestretching may alter its load-bearing structure and subsequent mechanical response [44,45]. Stable, repeatable loading–unloading curves after conditioning indicate a relatively stable response within the relevant operating range. Establishing a return to the untreated initial state requires comparison of initial loading, postconditioning loading, and retesting after a specified rest period. Unlike recovery after unloading an intact specimen, self-healing or repair after cutting requires the two cut surfaces to recontact and form connections; the extent of restored load transfer must then be verified. Repair in metal-coordinated gels and glycerol-containing gelatin gels involves recontact of the cut surfaces and corresponding waiting or treatment conditions [18,46]. Rebound after unloading, repeatable responses after training, and repair after cutting have different initial states and observables and should be evaluated separately. Structural damage that persists despite rest may continue to accumulate during subsequent repeated deformation.

### 2.4. Cracks and Fatigue

The ability of an intact hydrogel specimen to sustain large tensile deformation does not imply equal fracture resistance when a notch is present. A notch concentrates local stress and deformation at the crack tip, so crack resistance must be evaluated with the specimen's crack state specified. Fracture energy describes the energy required per unit of newly formed crack area under particular conditions. Classical tearing-energy methods use specimen geometry and loading conditions to determine fracture energy at the onset of crack growth, providing a basis for hydrogel fracture testing [33,47]. The input work density obtained by stretching an unnotched specimen to failure is normalized by initial volume and expressed in $J/m^3$, whereas fracture energy is normalized by new crack area and expressed in $J/m^2$. They represent different specimen conditions and physical quantities [48].

Network deformation and load redistribution near a crack tip can influence resistance to crack growth. Zhu et al. compared the deformation of notched traditional double-network (TDN) and highly entangled double-network (HEDN) hydrogels (Figure 3). Figure 3a,d shows their structural differences; Figure 3b,e uses polarized-light images at different extensions to record changes in notch shape; Figure 3c,f schematically illustrates network organization under stretching. Compared with the TDN gel, the HEDN gel develops pronounced orientation during stretching and exhibits notch-tip blunting. The authors associate this behavior with load transfer involving long-chain entanglements and chain rearrangement, proposing that these processes redistribute deformation near the crack tip and reduce local stress concentration [35]. Overall cyclic dissipation and crack resistance do not necessarily increase together. Wang et al. showed that low bulk mechanical hysteresis and high crack resistance can coexist in fiber-reinforced elastomer composites [48].

A material that does not fracture rapidly under a single loading event may nevertheless undergo gradual growth of an existing crack during repeated loading [49]. Fatigue tests commonly use precracked specimens, recording crack length $a$ against cycle number $N$ and examining crack-growth rate as a function of the energy release rate, $G$. Here, $G$ is the energy available for release per unit crack-extension area. Under specified cyclic conditions, the minimum energy release rate that sustains crack growth is termed the fatigue threshold [37]. Its determination also depends on observation time and crack-detection capability. When growth is very slow or below the detection limit, the absence of appreciable growth over a finite period does not prove that the crack has stopped advancing [37]. Lake–Thomas theory connects the intrinsic fracture-energy scale of elastic networks with polymer-chain

rupture, providing a theoretical basis for understanding fatigue in polymer networks [50]. In hydrogels, dynamic connections and reinforcing structures also participate in cyclic crack growth, so connection kinetics and network organization may alter the driving force required for propagation. Cyclic crack studies of dynamic networks and fatigue-resistant crystalline gels provide experimental evidence for these structural effects [37,51]. Fatigue thresholds should therefore be reported together with loading rate, environment, and measurement method. The number of cycles sustained by an intact, unnotched specimen is a different test result and cannot directly determine the fatigue threshold of an existing crack.

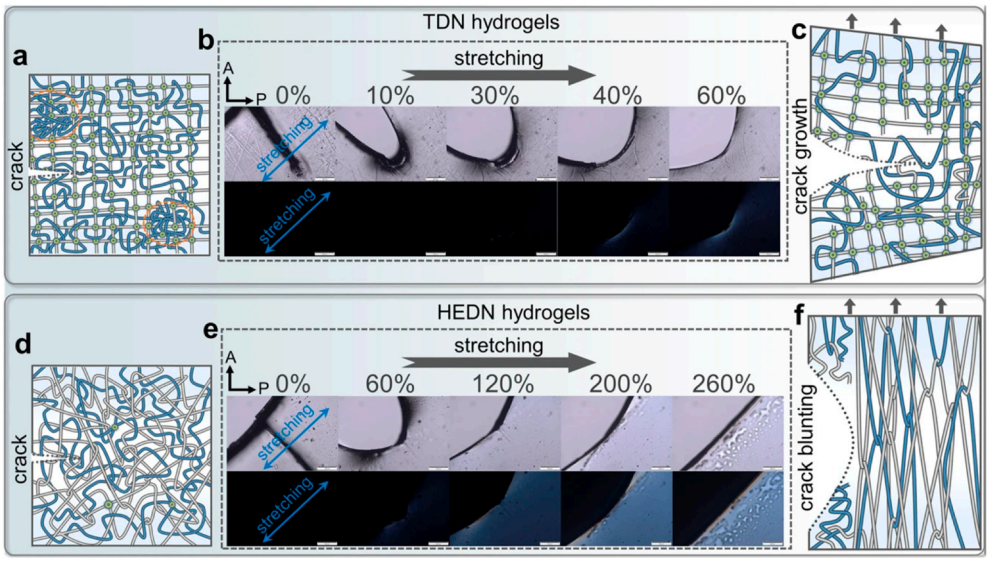



**Figure 3.** Crack blunting mechanism of HEDN hydrogels. Illustration of the network structure of the notched TDN (**a**) and notched HEDN (**d**) hydrogels. Polarized optical images of notched TDN (**b**) and notched HEDN (**e**) hydrogel with increasing strains, showing the absence of crack propagation. Photos with a white background are regular light microscope images, and those with a black background were taken in polarized mode. The stretching direction of the hydrogel samples forms a 45° angle with the direction of the polarizer and analyzer. The direction of A: analyzer, P: polarizer. Scale bars, 500 μm. Illustration of network structure for the notched TDN (**c**) and notched HEDN (**f**) hydrogels in the stretched state [35].

Cyclic damage develops at different stages and locations. Distributed local damage may precede a visible crack; after crack initiation, damage further manifests as observable crack propagation. Fatigue-initiation models must therefore distinguish crack-initiation life from the propagation life of an existing crack, and their predictions still require corresponding experimental validation [52]. In addition to bulk damage, interfacial cracks or delamination may develop between a gel and its electrodes, substrate, or encapsulation. Bonded interfaces have their own fracture behavior. Fatigue cracks along an interface follow paths distinct from cracks within the gel and require appropriate interfacial fatigue tests [53,54]. As bulk cracks or interfacial delamination develop, local load-bearing capacity, strain transfer between device components, and conductive connections may change. Cyclic evaluation of strain sensors must therefore observe cracks and delamination while examining whether deformation continues to reach the sensing region and whether the original strain–electrical-signal relationship is retained.

## 3. Strain-Sensing Mechanisms and Measurement Evaluation

### *3.1. Conduction and Strain Response*

The electrical response of conductive hydrogels arises from mobile charges and their transport pathways. Electronic conduction is carried by electrons or holes and can occur through contacts between conductive components, tunneling between adjacent conductive units, or hopping between localized electronic states. Ionic conduction relies on cation and anion migration through the aqueous phase, influenced by hydration and interactions with the polymer network. When both transport mechanisms contribute, the material exhibits mixed conduction; adding conductive fillers does not necessarily eliminate the existing ionic contribution [1,55]. Different components of a composite hydrogel can provide mechanical load bearing and charge transport. In the composite gel developed by Shen et al., PVA provides mechanical support while a conducting polymer forms charge-transport pathways [8]. In the cosolvent-containing composite gel studied by Bi et al., noncovalent interactions allow sheet-like fillers to reinforce the network, while interactions of the conducting polymer with PVA and the fillers establish a conductive network [56].

Conductive pathways can be built through different processing routes. Blending poly(3,4-ethylenedioxythiophene):polystyrene sulfonate (PEDOT:PSS) with PVA followed by freezing and thawing produces interlocked conducting and load-bearing phases [8], whereas polymerizing pyrrole within a preformed polyacrylamide matrix constructs the conducting phase sequentially [17]. Ionic pathways can instead be regulated by introducing mobile ions during preparation or subsequent equilibration of the hydrated network [57]. These approaches extend the design focus from adding charge carriers to controlling pathway continuity and its coupling to deformation. Phase interlocking, sequential construction, and spatial separation therefore offer complementary routes for coordinating transport with mechanical recovery [8,17,58].

Salt-containing aqueous gels provide mobile ions without requiring a particulate percolation network, but water exchange and ion redistribution can affect their electrical response [57,59]. Networks bearing ionizable groups or reversible metal coordination integrate ionic transport with network interactions, although ionic association and bond relaxation can also couple transport to mechanical history [18,60]. In conducting-polymer or filler composites, electronic continuity becomes an additional design variable: microphase interlocking can preserve conductive contacts, whereas filler-network rearrangement can contribute to electrical hysteresis [8,9]. For electrolyte use, ionic transport must be considered together with electronic leakage. A highly conducting electronic phase may benefit an electrode or resistive pathway but does not by itself establish suitability as an electrolyte. These distinctions favor matching network chemistry and carrier transport to the intended device function.

Electronic and ionic conduction describe charge-carrier mechanisms within a material, whereas resistance and capacitance are device readout quantities; there is no one-to-one correspondence between these classifications. Figure 4 connects charge transport with device operating modes. Resistive strain sensors generate electrical responses through deformation-induced changes in conductive pathways (Figure 4a). For a uniform conductor, bulk resistance follows $R = \rho\frac{L}{A}$, where $\rho$ is resistivity, $L$ is length along the current direction, and $A$ is the cross-sectional area perpendicular to that direction [6]. Under uniform uniaxial stretching with constant volume and resistivity, the stretch ratio $\lambda$ defined in Section 2 gives $\frac{R}{R_0} = \lambda^2$. Here, $R_0$ and $A_0$ are resistance and cross-sectional area in the same initial state. This relationship shows that increasing length and decreasing cross-sectional area alone can increase resistance. In real hydrogels, stretching may change the contacts, spacing, and orientation of conductive components, while hydration also affects charge transport; resistivity may therefore vary. The conducting polymer composite gel of Shen

et al. and the glycerol-containing gelatin gel of Hardman et al. both exhibit approximately linear resistance–strain responses within their respective tested ranges [8,46]. The actual resistance–strain relationship must therefore be established by calibration; the squared relationship is a geometric reference valid under its stated assumptions.

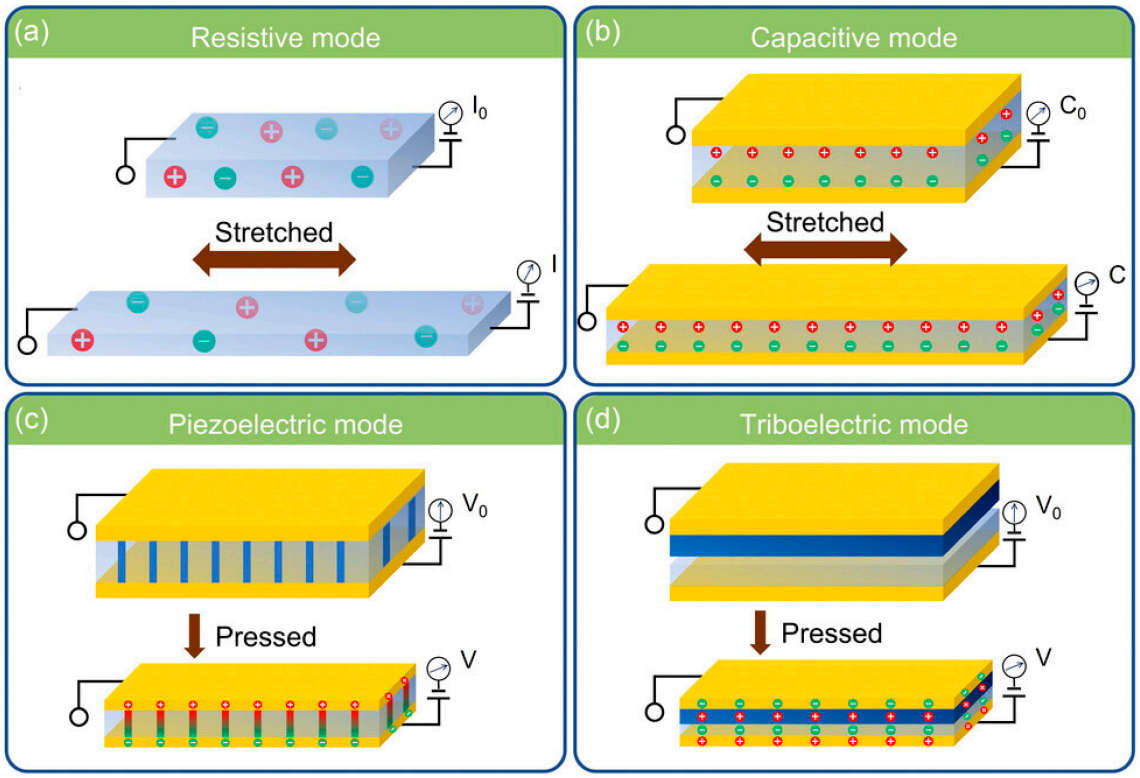



**Figure 4.** Schematic of structure and working mechanism of conductive-hydrogel-based strain/pressure sensors operated under (**a**) resistive, (**b**) capacitive, (**c**) piezoelectric, and (**d**) triboelectric mode [14].

Capacitive strain sensors generate output through deformation-induced changes in charge storage (Figure 4b). For an ideal parallel-plate capacitor, capacitance is $C = \varepsilon_0 \varepsilon_r \frac{A_{eff}}{d}$, where $\varepsilon_0$ and $\varepsilon_r$ are vacuum and relative permittivity, respectively, $A_{eff}$ is effective electrode overlap area, and $d$ is electrode separation. Changes in electrode area, separation, and dielectric state all affect capacitance. Beyond geometric capacitance, opposite charges may accumulate on either side of an ionic conductor–electronic conductor interface, forming an electrical double layer. In the absence of electrochemical reactions, Keplinger et al. represented charge storage in electrical double layers and an insulating dielectric layer as series capacitances, with the smaller dielectric-layer capacitance predominantly limiting the device's total capacitance [59]. Cao et al. used a different equivalent circuit for layered hydrogel fibers, comprising two interfacial double-layer capacitances and the bulk resistance of the middle layer, with a geometric capacitance in parallel with this branch [5]. Geometric capacitance, interfacial charge accumulation, and bulk transport may thus jointly contribute to device response. The equivalent circuit should be determined from the specific structure and interfacial processes. Figure 4c,d shows piezoelectric and triboelectric modes, respectively. Piezoelectric output arises from polarization of piezoelectric components under force, whereas triboelectric output involves electrostatic induction following contact electrification. Hydrogels can provide compliant conductive contacts in these devices [14].

### 3.2. Device Structure and Signal Readout

A conductive hydrogel strain sensor comprises a sensing body, electrodes, contacts, and, as required, a substrate and encapsulation. The sensing body deforms with the measured object and generates an electrical response; electrodes and contacts connect it to the external measurement circuit. The substrate provides support or a mounting interface, while encapsulation protects the gel and its connections and regulates water exchange with the surroundings. Device fabrication therefore involves both gel shaping and the connection and assembly of functional components [61]. Silicone rubber and acrylic elastomers can serve as protective encapsulation layers [8,9]. Cao et al. integrated conductive side layers and an intermediate hydrogel layer within a single fiber for capacitive strain readout [5]. After assembly, the layers generally deform together, and encapsulation thickness, compliance, and interlayer bonding also affect load transfer to the sensing body.

Externally imposed displacement is transmitted through grips, mounting interfaces, and the substrate before producing strain in the sensing region. The change in distance between two markers relative to their initial separation gives the average strain over that interval; localized deformation can make local strain differ from the overall average. Grip slip, interfacial adhesion, and stiffness differences between the gel and substrate all affect this transfer [2]. Actuator travel may include grip slip and deformation outside the gauge length and therefore need not equal actual extension within the gel's effective gauge length. During controlled stretching, Hardman et al. calculated strain from the gel's initial exposed length while measuring resistance concurrently; Meng et al. cyclically stretched specimens with an initial gauge length of 10 mm [4,46]. Mounting pretension also changes the initial device state. Calibration strain should therefore correspond to the actual sensing region. Where necessary, independent displacement measurements or image records should verify strain transfer and establish the mechanical input corresponding to the electrical output.

Electrical signals recorded by a measurement circuit may include contributions from the gel bulk, electrode contacts, and electrode interfaces. Under approximately resistive conditions, resistance can be characterized by the voltage-to-current ratio. When ions accumulate near electrodes, readings also depend on interfacial charging and discharging. At an ideally polarizable interface without electrochemical reactions, direct current cannot continue to flow after double-layer charging is complete [59]. Alternating-current (AC) readout measures impedance using periodic electrical excitation. Within the small-signal linear-response regime, impedance is characterized by the voltage-to-current amplitude ratio and phase difference at the same frequency, reflecting resistive and charge-storage processes. Hardman et al. used AC resistance readout to reduce the effects of unidirectional ion migration during short measurements [46]. Electrode material and applied bias also affect interfacial electrochemistry. Using aluminum-foil electrodes to measure iron-coordinated gels, Khodami et al. observed current falling to zero after application of a 3 V bias and attributed this to Faradaic reactions at the electrode interface [62].

Song et al. compared direct-current (DC) resistance and AC impedance readout in glycerol-modified, genipin-crosslinked gelatin gels (gelapin) and dopamine-functionalized poly(ethylene glycol) (PEG-Dopa). DC tests used a 10 μA current; AC tests used electrical excitation at 10 kHz and 20 mV (Figure 5). Figure 5a,b shows DC resistance responses, Figure 5c,d high-frequency impedance responses, Figure 5e,f the corresponding mechanical stress–strain cycles, and Figure 5g,h strain-response relationships over the respective tested ranges [63]. Where the DC curves show baseline drift or waveform distortion, high-frequency AC impedance curves exhibit clearer, more repeatable plateaus. Mechanical stress–strain loops remain, showing that mechanical dissipation and path differences in high-frequency electrical readout do not necessarily vary together. Test amplitudes must also be distinguished: both readout modes used step strains of 15% and 30% for gelapin;

for PEG-Dopa, DC tests used 15% and 30%, whereas high-frequency AC tests used approximately 50% and 100%. These results cannot all be treated as single-variable comparisons that change only readout mode at identical strains. The measured electrical signal depends jointly on the material, mechanical input, and electrical excitation.

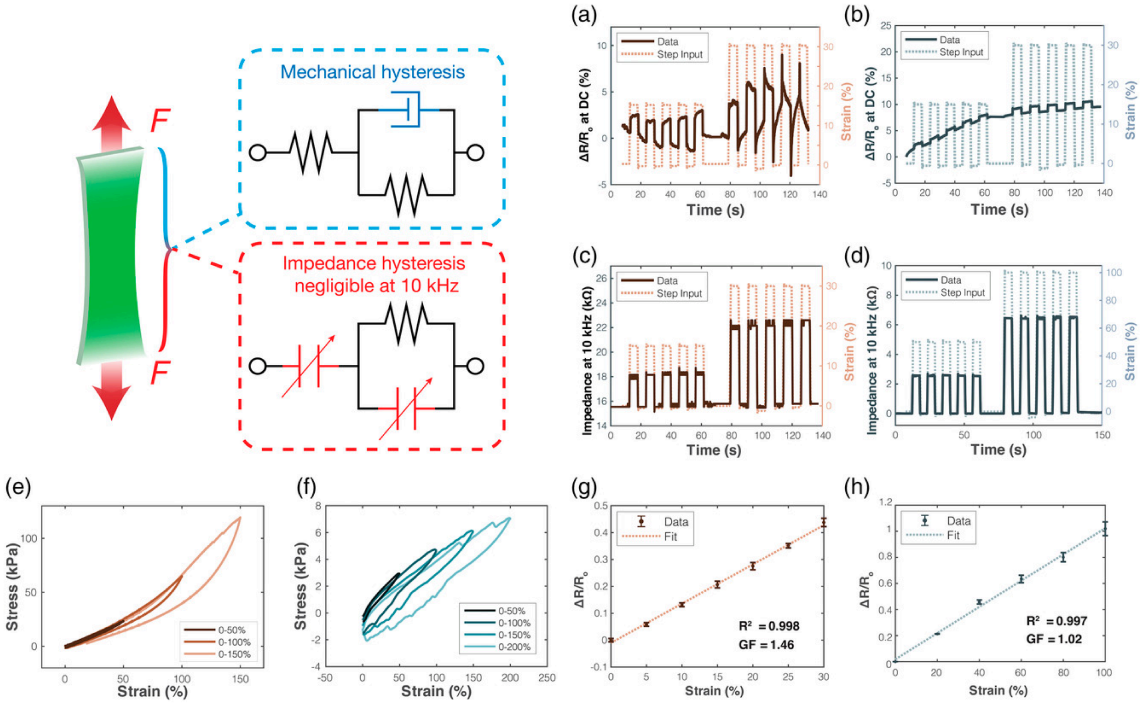



**Figure 5.** Comparison of electromechanical properties of genipin-crosslinked gelatin (gelapin) and PEG-Dopa using the DC resistance method and the high-frequency impedance-based method. (**a**,**b**) The DC resistance response to step input strains of 15% and 30% for (**a**) gelapin and (**b**) PEG-Dopa. (**c**,**d**) The 10 kHz impedance response to step input strains of 15% and 30% for (**c**) gelapin and (**d**) PEG-Dopa and its linearity for (**g**) gelapin and (**h**) PEG-Dopa. (**e**,**f**) Stress–strain cycles at various strains for (**e**) gelapin and (**f**) PEG-Dopa [63].

Device measurement involves three distinct temporal processes: mechanical loading, electrical excitation, and data acquisition. Mechanical loading frequency is the number of deformation cycles per second, while loading rate describes how quickly strain changes. Electrical excitation frequency is the frequency of the periodic probing signal applied by the measurement circuit; sampling frequency is the number of data points recorded per second. These parameters describe the timing of mechanical input, electrical probing, and signal recording, respectively. Hardman et al. used AC resistance readout during controlled stretching, demonstrating concurrent mechanical deformation and electrical measurement. Meng et al. recorded current waveforms at different mechanical loading frequencies, demonstrating the effect of loading schedule on dynamic signals [4,46]. Smoothing, such as moving averages, can suppress rapid fluctuations but may attenuate signal peaks or introduce delays. Circuit bandwidth limits the signal-frequency range that can be recorded accurately [6]. A common time base for mechanical input and electrical output, together with specified loading rate, electrical excitation, sampling frequency, filtering, and circuit bandwidth, provides the basis for interpreting signal changes and their timing differences.

### *3.3. Calibration and Dynamic Response*

Calibration establishes the correspondence between known strain and electrical output. Resistive sensors commonly use relative resistance change, $s$, whereas capacitive sensors use

relative capacitance change, expressed as $s = \frac{R-R_0}{R_0}$ and $\frac{C-C_0}{C_0}$, respectively. Here, $R$ and $C$ are the currently measured resistance and capacitance, and $R_0$ and $C_0$ are their values in a specified reference state. Recording actual strain and electrical output together during controlled stretching provides paired strain–signal data for fitting a calibration relationship [8,46]. This relationship depends on the material as well as initial strain, mounting, environment, and precycling history. The same specimen may produce different outputs at the same strain under different mounting or environmental conditions [6]. Calibration must therefore specify its reference state and applicable conditions. New electrical signals can then be used to estimate strain within the range where the relationship remains valid and uniquely invertible. Fitting and independent validation serve different purposes: fitting establishes the relationship using known strains and their signals; validation uses known strains excluded from fitting, estimates strain from electrical output, and compares the estimates with the applied values to evaluate measurement error.

Sensitivity describes how electrical output changes with strain. For resistive strain sensors, the gauge factor (GF) commonly relates relative resistance response to engineering strain: $\mathrm{GF} = \frac{s}{\varepsilon}$, where $\varepsilon$ is dimensionless engineering strain. This ratio gives the average response change per unit strain from the reference state to a specified strain; the local sensitivity of a nonlinear response is given by $\frac{ds}{d\varepsilon}$. Slopes from piecewise fits must be accompanied by their strain intervals [8]. Working range and linearity also determine which measurement tasks a sensor can perform [64]. Figure 6 illustrates combinations of linearity, nonlinearity, monotonicity, and hysteresis. In Case 1, loading and unloading paths coincide and the response is linear. Case 3 is nonlinear but strictly monotonic, allowing strain estimation using its inverse function. In Case 4, different strains on opposite sides of the curve's maximum give the same output; determining strain then requires selecting a monotonic branch or adding state information [65]. Linearity and unique invertibility are different properties, so nonlinearity alone does not preclude calibration. The smallest resolvable strain change also depends on noise and signal processing, whereas measurement accuracy requires assessment of strain-estimation error against an independent strain reference [6]. Within the same small-strain interval, a larger absolute GF gives a larger relative resistance change, but noise, drift, and departures from the calibration curve still affect readings. High GF therefore does not necessarily imply high accuracy, and a high fitted coefficient of determination, $R^2$, cannot replace independent validation of measurement error.

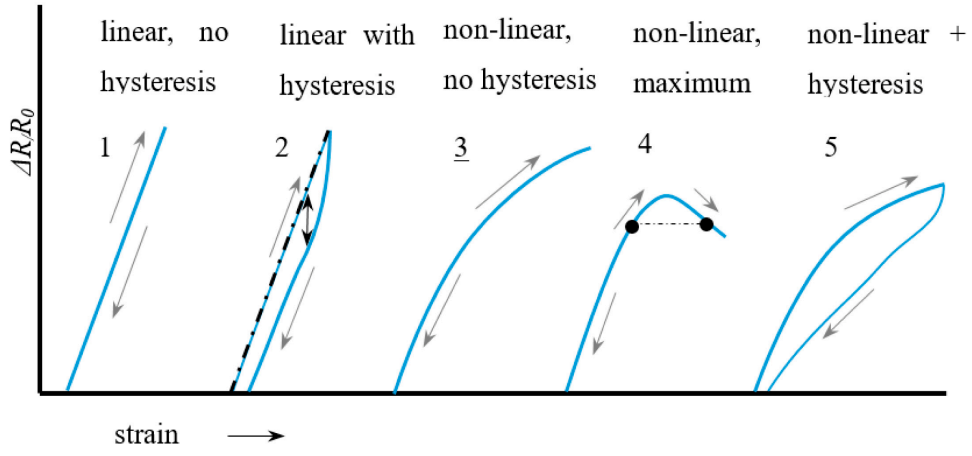



**Figure 6.** Nonlinearity and hysteresis examples [65].

The strain–signal relationship may also depend on loading direction. Cases 2 and 5 in Figure 6 show hysteresis superimposed on linear and nonlinear responses, respectively: the same strain can produce different outputs during loading and unloading. Within the output

range shared by the two branches, estimated strain also depends on motion direction [65]. Such path differences relate to the history dependence of materials and interfaces. Network relaxation changes chain conformation and local constraints over time, with transient-entanglement studies providing a mechanical basis for this time dependence [38]. If these changes alter contacts or spacing between conductive units or the environment for ion migration, transport pathways during unloading may differ from those during loading [1]. Ion redistribution, electrode polarization, and changes in hydration may also contribute to electrical-output differences [46]. These processes need not coexist in every device; appropriate control experiments are required to identify dominant mechanisms. Mechanical and electrical loops record different physical quantities, so their hysteresis fractions cannot be directly converted. Unsynchronized acquisition of mechanical input and electrical output or filtering delays may also create apparent loading–unloading branch differences and must be distinguished from the actual temporal responses of materials and interfaces [6].

Electrical hysteresis quantification depends on which branch differences are compared and how they are normalized. Area-based metrics describe overall path differences across the test interval. Shen et al. used the difference between areas under loading and unloading resistance-response curves relative to the loading area [8]. Jansen et al. separately defined vertical and horizontal hysteresis: vertical hysteresis compares branch resistance differences at equal strain, normalized by resistance output span; horizontal hysteresis compares branch strain differences at equal output, normalized by strain span [65]. A maximum-deviation metric instead takes the largest absolute output difference between branches over a specified strain interval and divides it by a defined output span, indicating the worst local deviation. If loading and unloading curves cross, signed area differences may underestimate local path differences because positive and negative contributions cancel. The area of an electrical-signal–strain loop measures output-path differences, not mechanical work or mechanical dissipation. Hysteresis also depends on maximum strain amplitude; for example, the conductive alginate composite gels studied by Sharabr Sembiring et al. exhibit different hysteresis responses at different maximum strains [66]. Comparisons must therefore harmonize or explicitly state the calculation definition, normalization, reference state, strain amplitude, loading rate, and cycle state.

Dynamic response describes whether a sensor follows time-varying mechanical input promptly. Step tests require synchronized recording of actual strain and electrical output, with defined start and end points and signal-change fractions for response and recovery times. The interval from the onset of input change to the first detectable electrical change describes the onset delay; the subsequent interval between two specified signal thresholds describes completion of the defined signal transition [6]. Periodic tests compare input and output amplitudes, phases, and waveforms to evaluate tracking during continuous motion. Phase difference describes how far output leads or lags input within a cycle. Current records from Meng et al.'s nanoparticle-reinforced hydrogels and capacitance records from Cao et al.'s layered hydrogel fibers illustrate dynamic responses at different mechanical loading frequencies [4,5]. At fixed loading frequency and waveform shape, increasing strain amplitude also increases strain rate. Dynamic performance therefore cannot be evaluated from loading frequency alone; signal error should be assessed at specified strain amplitudes and frequencies. The measured temporal response depends jointly on the loading equipment, the material, and signal processing in the measurement circuit. Recovery of material deformation and recovery of electrical signals are different observables.

### *3.4. Cyclic Measurement and Reliability*

Assessing stability during cyclic measurement requires considering baseline, peak-to-peak amplitude, sensitivity, and hysteresis together. Baseline is output at a specified

reference strain; peak-to-peak amplitude is the difference between maximum and minimum output within a cycle. The slope of the output–strain curve indicates sensitivity, while differences between loading and unloading branches indicate hysteresis. Systematic changes in baseline or response relationship over time constitute drift, whereas random fluctuations at fixed input constitute noise. Short-term repeatability concerns agreement among repeated measurements under the same conditions; long-term stability concerns retention of baseline and the output–strain relationship over time or cycles [6]. These metrics need not vary together. Han et al. observed relatively stable cyclic amplitude and waveform despite drift of the entire signal trajectory, demonstrating that amplitude and waveform retention do not establish baseline stability [10]. Choi et al. evaluated signal retention through sustained cycling of individual devices and response consistency by comparing independent devices [9]. Reliability evaluation should therefore retain continuous records referenced to the original state and compare complete response curves at necessary checkpoints, rather than judge waveform repetition from a few selected cycles. Many cycles on one device cannot replace consistency testing across independent devices.

Whether the original calibration remains usable after cycling is central to reliability. Validation uses the original precycling reference values and fitted parameters to independently test known strains after cycling or a specified rest period. Strains estimated from electrical output are compared with the applied values. Errors remaining within task-specific limits indicate that the original calibration remains valid under those validation conditions [6]. Rezeroing corrects the output reference when the baseline shifts; refitting is required when the strain–output relationship itself changes. These corrections should be reported separately and distinguished from results obtained by directly retaining the original calibration. In Hardman et al.'s glycerol-containing gelatin gels, environmental changes could alter baseline resistance while relative sensitivity remained similar, requiring the reference value to be reestablished as appropriate [46]. Retention of relative response therefore does not imply retention of the original baseline. Likewise, resistance or capacitance returning to its initial value after unloading indicates recovery only of that reference point. Establishing recovery of measurement capability also requires checking response slopes, loading and unloading paths, and dynamic-response characteristics across the working range.

Failure criteria for cyclic reliability must follow the measurement task. Bulk cracking, interlayer delamination, and electrical disconnection can all affect device operation. Interfacial cracks have their own propagation behavior and should be observed separately from bulk gel damage [53]. Measurement failure may involve loss of electrical output, inability to cover the specified strain range, or errors exceeding task limits under the specified calibration procedure. Failure should therefore be judged by whether the device can perform its assigned measurement task, rather than solely by visible material cracks [6]. Mechanical and sensing cycles also probe different quantities. For example, Cao et al. separately tracked load-bearing capacity and capacitance response in layered hydrogel fibers to evaluate mechanical and electrical retention [5]. If a test ends before the predefined failure condition is reached, the reported cycle count indicates only the cycles completed under those conditions and does not directly establish the actual lifetime to failure. Pauses, rehydration, and recalibration are also test conditions that must be considered. Connecting material recovery, signal retention, and sustained measurement under the same operating conditions is necessary to determine which functions a structural design preserves and whether they meet practical requirements.

## 4. Progress Toward Toughness, Low Hysteresis, and Cyclic Reliability

### 4.1. Dissipation and Recovery of Load-Bearing Networks

Repeated load bearing requires hydrogel networks to relieve local stress through internal structural adjustment during stretching and recover load-bearing capacity after unloading [67]. In silver–polydopamine dynamic networks, Shi et al. found mechanical hysteresis of 5.2% for a preferred formulation and 19.3% for a high-strength formulation. Within that formulation comparison, increased strength was accompanied by greater cyclic dissipation [68]. Mechanical quantities also recover to different extents after unloading. After 500% strain followed by 7 min of rest, Huang et al.'s hydrophobic–ionic hyaluronic acid network recovered 99.45% of peak stress, 99.9% of elastic modulus, and 68% of dissipated energy [7]. After 10 min of rest, Wu et al.'s fully physical double network recovered 57.08% of dissipated energy and 99.06% of peak stress [69]. Although the material systems and rest conditions differ, peak load-bearing capacity recovered more fully than dissipative capacity in both studies.

Network connectivity and waiting time after unloading jointly influence recovery of these mechanical quantities. At 200% strain, the metal-coordinated network studied by Ghosh et al. had a loading work density of approximately 52 kJ/m$^3$, of which approximately 22 kJ/m$^3$ was not returned during unloading. Longer rest after cycling increased recovery of dissipated energy, indicating that reversible coordination structures require time to reorganize [18]. Liang et al. maintained network integrity through microgel-particle deformation, chain entanglement, and covalent connections, while hydrophobic associations provided reversible dissipation. After five consecutive cycles at 500% strain, 5 min of rest restored the mechanical loading–unloading curves to a similar state [70]. Sun et al. introduced hydroxyl-rich diol nanocellulose into a polyacrylamide network, using reversible hydrogen bonds to regulate network connections, and reported low mechanical hysteresis together with retention of mechanical and sensing performance after cycling [71]. Recovery thus depends on the reversible connections, the quantity examined, the rate of structural reorganization, and the actual intervals between cycles. Intermittent measurement can use pauses to promote network rebuilding, whereas rapid continuous measurement requires sufficient structural stability between successive cycles.

Beyond rebuilding after unloading, movable crosslinks can redistribute chain forces during loading. Huang et al.'s polyrotaxane network allows crosslinks to move along threaded chains while a covalent network maintains overall integrity [11]. Crosslink motion changes the effective lengths of adjacent network strands and redistributes local tension. Figure 7 shows higher strain at break, fracture energy, and tensile toughness than in two control groups. During cycling at 100% strain, peak stress indicates better retention of load-bearing capacity after early adjustment. The study also reports mechanical hysteresis below 8% after the first cycle and input-work retention of approximately 80% after 100 cycles, compared with 58% and 41% for the controls. Low hysteresis ratios were also observed across strain ranges of 50–800% [11]. Movable crosslinks therefore participate in energy dissipation at large deformation while improving subsequent load bearing through tension redistribution. The extent of this improvement depends on strain amplitude and loading history.

Xiong et al. similarly introduced movable junctions into a printable pseudorotaxane network to redistribute stress. They separately reported mechanical cycling at 300% strain and 100 electrical-signal cycles; the complete material also contains ethylene glycol and a choline salt [72]. Unlike crosslink motion, highly entangled double networks distribute load through topological connections between long chains. At 200% strain and 500 mm/min without pauses between cycles, Zhu et al. measured a second-to-first-cycle loading-work ratio of approximately 99%, compared with approximately 33% for a traditional double-

network control. This ratio indicates retention of load-bearing capacity in the subsequent cycle, not return of 99% of the energy within each cycle [35]. Sliding entanglement islands formed by MXene sheets and long polyacrylamide chains instead alleviate local stress concentration by transferring stress to neighboring chains [73].

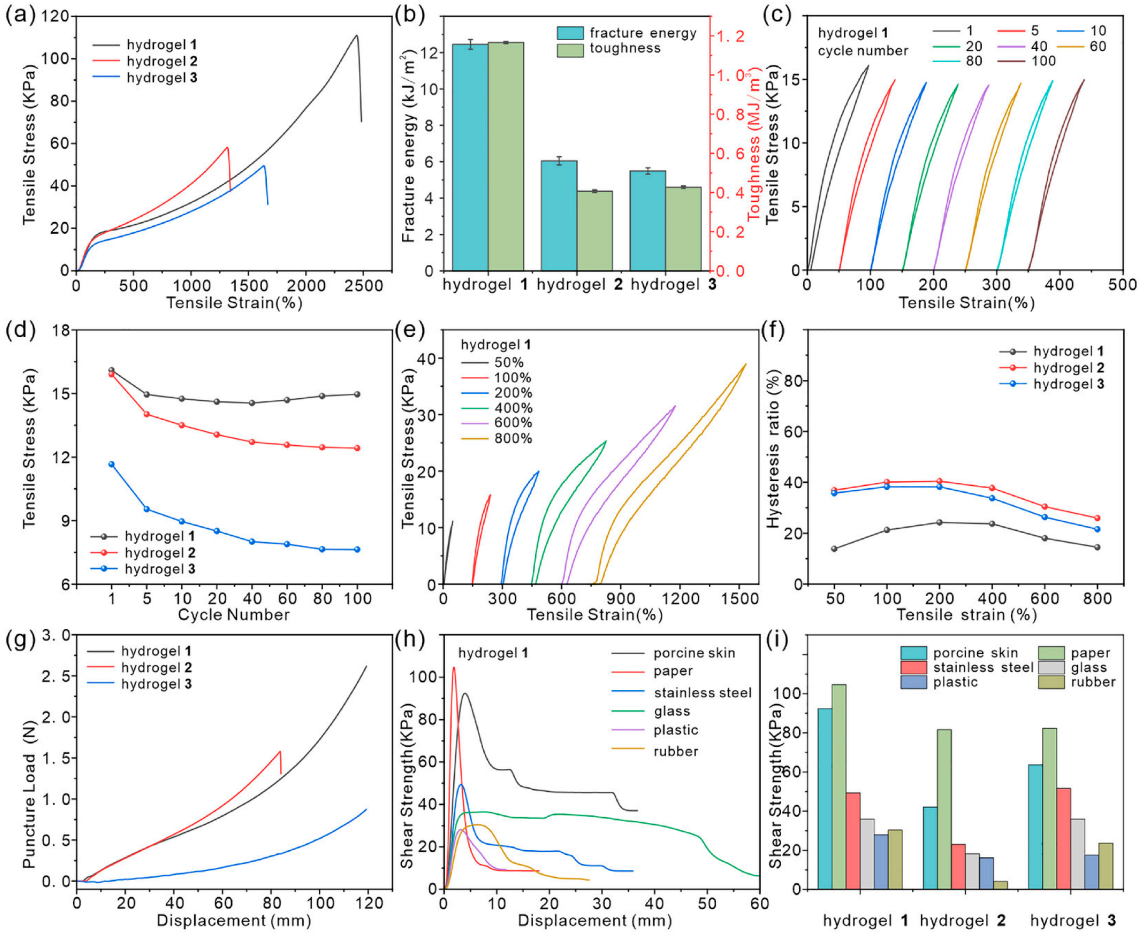



**Figure 7.** Comparative mechanical properties of the hydrogels 1, 2, and 3. Representative tensile stress–strain curves (**a**) and corresponding fracture energy and toughness (**b**) of the hydrogels 1, 2, and 3. (**c**) Successive cyclic loading–unloading curves of hydrogel 1 at 100% strain for 100 cycles. (**d**) The tensile stress change trends of hydrogels 1, 2, and 3 at 100% strain for 100 cycles. (**e**) Loading–unloading tensile curves of hydrogel 1 at different strains from 50% to 800%. (**f**) Comparison of the hysteresis ratio change trends of hydrogel 1, 2, and 3 at varying strains from 50% to 800%. (**g**) Puncture force versus displacement curves of the hydrogels 1, 2, and 3. (**h**) Adhesive shear strength versus displacement curves of the hydrogel 1 to various substrates. (**i**) Comparison of the adhesive shear strength of the hydrogels 1, 2, and 3 to various substrates [11].

Particle connections also alter chain constraints and the space available for chain motion. Meng et al. combined nanoparticle connection topology with a water content of 96% to reduce transient chain constraints and allow greater chain mobility. The material completed 5000 mechanical cycles at a stretch ratio of 4 in a water bath [4]. Liu et al.'s topologically entangled network containing ZIF-8 nanoparticles showed pronounced strain-amplitude dependence: mechanical hysteresis increased from 5.45% to 8.8% as stretch ratio increased from 2 to 5 [74]. Movable connections, long-chain entanglements, and particle constraints all influence load distribution, but act through junction relocation, interchain topological connections, and regulation of chain mobility, respectively. Design must coordinate movable connections with a stable framework to maintain both structural integrity and repeated load bearing within the target strain range.

Hydration and microphase organization further affect chain mobility and local forces. Wang et al. adjusted differential hydration of salt and polymer in a polyacrylamide–calcium chloride system, changing the balance of bound and free water. They attributed reduced mechanical dissipation to spatial confinement, chain sliding, and alleviated stress concentration; mechanical hysteresis was 0.13% at 1000% strain [75]. Zhang et al. used arrested phase separation to construct a hydrophobic load-bearing phase and a hydrophilic elastic phase. The former carried the main load, while the latter helped alleviate local stress concentration within it; chain entanglements restricted further phase coarsening. A specimen containing 75.6 wt% water exhibited 16.6% mechanical hysteresis at a stretch ratio of 2, showing that cooperative interphase load bearing coexisted with cyclic dissipation [28]. Wang et al. adjusted cellulose–nanocrystal hydration to suppress excessive phase separation and associated this with retained flexibility and improved crack resistance [76]. Zhou et al. organized a network of cell-like microgels, maintaining repeated load bearing through reversible particle deformation and connections while dissipating energy through particle splitting and aggregation at large deformation. Their base formulation exhibited mechanical hysteresis of 4.7% and 7.5% at 300% and 1300% strain, respectively [77]. These approaches regulate chain motion and local stress differently. When salt concentration, polymer concentration, and phase structure change together, performance improvements must be interpreted in terms of the complete material state and cannot be assigned to hydration or phase separation alone without independent controls.

Ordered structures may change reversibly during loading and unloading or persist as stable load-bearing units. Earlier work by Liu et al. found reversible crystallization during stretching of slide-ring poly(ethylene glycol) gels and crystal melting during retraction, demonstrating that loading-induced crystallization can reinforce a network [32]. Cao et al. introduced entangled sodium polyacrylate chains into layered hydrogel fibers, enabling reversible strain-induced crystallization, which they related to elastic recovery. During cycling at 200% strain, load-bearing stress decreased slightly over approximately the first 3000 cycles and then stabilized [5]. The cellulose–nanocrystal clusters used by Sun et al. oriented during stretching and returned to isotropy after unloading; the authors associated this change with an expanded stress-transfer region [78]. These studies all use loading-induced ordering, but polymer crystallization and melting are structurally distinct from the reversible orientation of nanocrystal clusters.

Stable reinforcement instead relies on persistent load-bearing units. Wu et al. used hydrothermal annealing to form PVA crystalline regions that carried load together with chain entanglements. Liang et al. combined bidirectional freeze casting, compression, and annealing to build hierarchical structures and reduce fatigue weaknesses associated with unidirectional orientation [79,80]. Such structures transfer load and obstruct crack growth without reforming after each unloading event. Reversible ordering depends on operating strain, whereas load transfer through stable reinforcement depends on loading direction. The directional consistency reported by Liang et al. applies mainly to in-plane directions and cannot be extended directly to all directions.

Applying these designs to strain sensing requires evaluating load bearing and recovery under actual measurement conditions. Fang et al. compared a highly entangled polyacrylamide network with a system containing an additional brittle agar network. The latter had higher modulus and mechanical hysteresis, whereas the former showed better signal sensitivity and stability in that study, indicating system-dependent trade-offs among stiffness, dissipation, and repeated sensing [81]. Lu et al.'s hyperelastic zwitterionic network showed incomplete length recovery as deformation increased, indicating a strain-amplitude limit to shape recovery [82]. After Si et al. introduced metal dendrites, both fatigue threshold and mechanical hysteresis increased, showing that improved crack-growth resistance can accom-

pany greater cyclic energy loss [83]. Material and device results must also be distinguished. Meng et al.'s dynamic current tests provide device-response evidence over specific frequencies, whereas Cao et al. separately reported mechanical and capacitive-response cycling of hydrogel fibers [4,5]. Huang et al. reported approximately 2% mechanical hysteresis at 100% strain and stable strain-sensor performance over 500 cycles under the reported sensing conditions [84]. Continuous or intermittent sensing relies on stable load-bearing capacity and electrical responses at the intended strain amplitudes and loading rates, with structural recovery matched to the intervals between loading events.

### *4.2. Rearrangement and Recovery of Conductive Pathways*

In hydrogels containing electronically conducting phases, load-bearing network recovery must be coordinated with conductive-pathway retention. Interphase connections, framework pretreatment, and the order of conductive-phase introduction provide distinct controls. Shen et al. interconnected a PEDOT:PSS conducting phase with a PVA load-bearing phase and attributed low electrical hysteresis to suppressed interphase sliding and separation. Using their area-based calculation, electrical hysteresis at 100% strain was $0.95 \pm 0.43\%$ across five samples [8]. Cao et al. instead modified deformation history by prestretching the PVA and ethylene–vinyl alcohol copolymer framework of a polypyrrole composite network. After treatment, strain readings during loading and unloading agreed more closely, whereas untreated controls retained differences, indicating that framework pretreatment affects composite strain response [85]. Li et al. used sequential construction: a highly entangled polyacrylamide network with good mechanical reversibility was formed first, followed by polypyrrole introduction, separating framework construction from conductive functionalization. Mechanical hysteresis was measured at 50% strain, while 500 sensing cycles at 30% strain separately assessed electrical repeatability [17]. These examples connect cyclic conductive-pathway retention with framework connectivity, deformation history, and construction sequence.

The internal state of the conducting phase and interactions between polymers provide additional ways to regulate composite deformation. Prameswati et al. post-treated PVA/PEDOT:PSS with sodium chloride and associated performance changes with stronger interphase interactions and altered PEDOT conformation, identifying the conducting phase's internal state as another design variable [86]. In all-polymer networks, Wang et al. combined hydrogen-bond clusters with electrostatic interactions between a poly(ionic liquid) and PSS. Xu et al. used hydroxypropyl methylcellulose to strengthen hydrogen-bond connections between PEDOT:PSS and polyacrylamide. Both maintained network connectivity through interpolymer interactions; their reported low mechanical hysteresis indicates limited energy loss during load bearing [87,88]. These designs extend control from interphase connectivity to interpolymer interactions and conducting-phase structure. In systems containing both conducting polymers and aqueous ions, both may contribute to charge transport, so the way network changes are reflected in sensing signals also depends on the readout mode.

Design of ionically conducting hydrogels must consider both network deformation and the environment for ion migration. Wu et al. used zirconium-ion–carboxyl coordination to lock highly entangled networks, providing ionic strain sensing while preserving fiber elastic recovery and load-bearing capacity. Mechanical hysteresis was 11% at 200% strain; the study also reported electrical hysteresis of 1.15% for the strain sensor. These metrics describe energy loss during load bearing and differences between electrical loading and unloading paths, respectively [89]. Zhao et al. adjusted the pH of a polyacrylamide/methylcellulose/silk fibroin triple network, jointly changing hydrogen bonding, pore structure, and ion transport. Ionic conductivity increased from 0.34 to 0.57 S/m, and wireless motion detection was demonstrated [90]. Wang et al. anchored polymer chains with modified starch and

introduced lithium chloride for ionic conduction, combining chain constraints with mobile ions and demonstrating device operation through repeated strain monitoring [91]. These studies connect load-bearing design with ion transport through coordination locking, pH adjustment, and chain anchoring, respectively.

The response of an ionic network must also be considered under its readout conditions. Song et al. measured aqueous PEG-Dopa gels using DC resistance and AC impedance separately. Under DC conditions, 15% and 30% strain steps accompanied continuous baseline drift. Under AC excitation at 10 kHz and 20 mV, impedance signals corresponding to approximately 50% and 100% strain in the original figure were relatively stable, with no observed hysteresis [63]. The tests used the different conditions described in Section 3.2. Apparent stability in ionic networks depends jointly on mechanical input, electrode processes, and electrical excitation.

Coordination of load bearing and conduction also depends on their spatial arrangement. Bulk composites make different components deform together within one material, whereas layered structures assign load bearing, electrode function, and charge storage to distinct units. In bulk composites, the PEDOT:PSS/PVA system discussed above connects load-bearing and conducting phases through microphase interlocking [8]. Liu et al. combined a conventional polyacrylamide network with a highly entangled conductive polyacrylamide network to coordinate fatigue-resistant structure with resistive response. They separately reported low-hysteresis behavior of the material and device and demonstrated applicability to periodic deformation monitoring through 500 cycles of resistance tracking in an ex vivo porcine-heart simulation [92]. Zhang et al. constructed microphase-interlocked networks in three-dimensionally printed PVA/conductive-carbon-black gels, using polydimethylsiloxane as the substrate and encapsulation. At 100% strain, relative force and resistance changes were recorded concurrently over 10,000 continuous cycles, allowing load-bearing behavior and resistive output to be compared under the same loading conditions [93].

Layered structures distribute electrical functions among different units. Cao et al. developed capacitive fibers with symmetric layered cross sections: a hydrated sodium polyacrylate middle layer, conductive side layers containing multiwalled carbon nanotubes that act as electrodes, and interfacial charge storage contributing to strain response [5]. Zhang et al. constructed an island–bridge carbon-nanotube coating on an ionically conducting organohydrogel, regulating AC impedance through structural changes in the electronically conducting surface and ionic bulk [58]. The bulk composites discussed above mainly generate resistance changes through deformation of conductive pathways. Layered fibers generate capacitance changes through combined deformation of electrodes, ionic layers, and interfaces, while the island–bridge coating and ionic bulk jointly influence AC impedance. Even when functions are spatially separated, loads still pass through phase or interlayer interfaces, so connection states continue to affect coupled mechanical–electrical responses.

Conductive-pathway recovery also includes the special case of reconnection after damage. Li et al. introduced phytic acid, boric acid, lithium chloride, and $Fe^{3+}$ into a polyacrylamide/chitosan system to form PCPBL@$Fe^{3+}$ hydrogels with hydrogen bonding and coordination interactions. Figure 8A shows a piecewise strain response over 0–1300%, with GF increasing from approximately 1.34 to 4.93. Figure 8B,C shows repeatable responses at 2–30% and 100–400% strain, respectively. Figure 8D gives response and recovery times of 0.11 and 0.20 s. Figure 8E shows 500 cycles at 50% strain and a stretching speed of 200 mm·min$^{-1}$, while Figure 8F relates finger-bending amplitude to resistance change. Beyond these cyclic and motion responses, Figure 8H shows a marked resistance increase after cutting and recovery to near the initial level after the cut surfaces recontact. The authors attribute this to reversible hydrogen bonding and coordination promoting interfacial recon-

nection and restoring ionic transport pathways. Figure 8G, however, shows conductivity declining during storage from approximately 9.72 S/m initially to approximately 2.25 S/m after 15 days. Electrical connectivity recovers when the cut surfaces are brought back into contact, whereas conductivity decreases during storage [94].

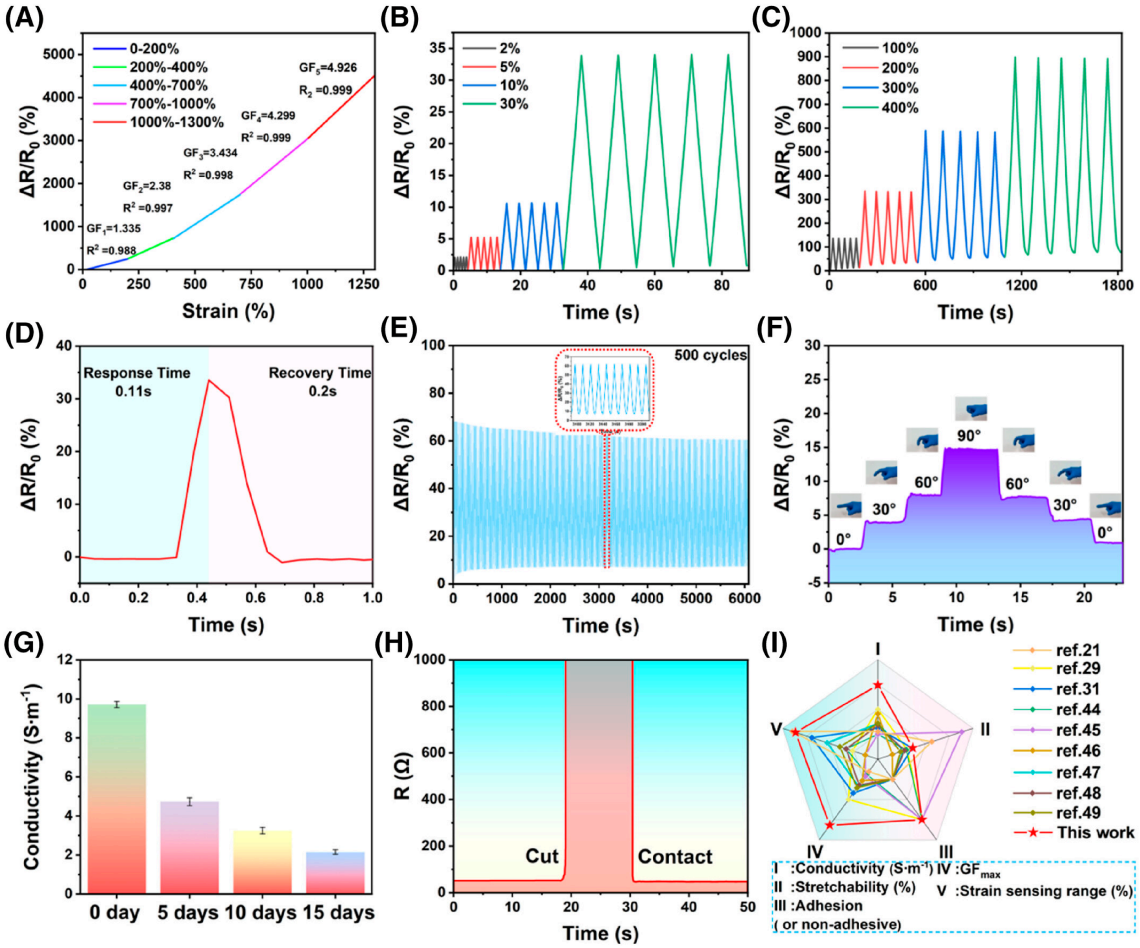



**Figure 8.** Electrical properties of PCPBL@$Fe^{3+}$ hydrogel. (**A**) Change in relative resistance of PCPBL@$Fe^{3+}$ hydrogel with the increase in tensile strains. Sensing performance at (**B**) low strain and (**C**) high strain. (**D**) Response time and recovery time. (**E**) Cycling stability test over 500 cycles at 50% strain and a stretching speed of 200 mm·$min^{-1}$. (**F**) Resistance change rate under different amplitude of finger bending. (**G**) Conductivity change under different number of days of placement. (**H**) Resistance change after hydrogel cutting and contacting. (**I**) A comparative analysis of the conductivity, stretchability, adhesion, gauge factor, and strain sensing range between the present study and the existing literature, presented via a radar chart [94].

After pathways reconnect, the extent to which electrical connection, load-bearing capacity, and the strain-measurement relationships recover must be assessed separately. In Liu et al.'s polyaniline–poly(acrylic acid) network, resistance returned close to its initial state approximately 11.6 s after cut surfaces recontacted. Mechanical strength recovery was 86.2% after 24 h at 25 °C. These results characterize electrical reconnection and load-bearing recovery, respectively, and correspond to different recovery processes. The same study also observed slight resistance-baseline shifts during 100 cycles at 100% strain [95].

During cycling without cutting, amplitude, baseline, and loading–unloading paths may likewise be retained to different extents. Han et al. found relatively stable signal amplitude and waveform after 1000 cycles at 10% strain, while the entire signal trajectory drifted, distinguishing response-shape retention from baseline retention [10]. Choi et al.'s encapsu-

lated devices produced repeatable outputs at 25% strain but retained appreciable loading–unloading hysteresis. Repeatable paths therefore do not imply the same strain–signal correspondence during loading and unloading [9]. Zhang et al. reported signal retention above 90% after 2600 cycles at 55% strain in a system combining nanophases and dynamic connections. This demonstrates substantial retention of signal output during prolonged cycling but cannot be directly converted into strain measurement error below 10% [96]. Evaluating postcycling measurement reliability therefore requires examination of baseline position, response slope, and differences between loading and unloading paths to verify whether the original calibration still meets operating requirements. Conformal measurement additionally requires evaluation of strain transfer across device interfaces.

### *4.3. Coupling and Stability of Device Interfaces*

Conformal strain sensors must first transfer deformation of the measured object into the gel. Adhesion maintains attachment and affects the actual strain experienced by the sensing region. Cao et al. used an adhesive PEDOT:PSS/polyacrylamide–sodium alginate gel for wireless motion capture at large deformation, demonstrating motion sensing while attached [97]. Wei et al. combined a PVA/phytic acid network with a second network, obtaining both adhesion and a relatively linear electrical response over 0–300% strain [98]. These studies demonstrate attached motion monitoring and controlled tensile response, respectively. Relating those outputs to actual object deformation additionally requires the interfacial strain-transfer relationship; motion waveforms alone do not establish the fraction of skin strain transferred to the gel.

Debonding controls clarify the influence of contact retention on output. In anionic–zwitterionic gels studied by Lee et al., a control lacking the relevant zwitterionic component detached from skin and produced unstable output, linking contact retention with signal differences [60]. Han et al.'s adhesive antiswelling gels nevertheless exhibited baseline drift during repeated stretching, showing that adhesion and swelling resistance alone do not ensure a stable electrical reference state [10]. Contact retention and baseline retention are different outcomes and cannot be summarized by one adhesion metric. Adhesion energy characterizes interfacial bonding, whereas controlled tensile response characterizes device behavior under a given mechanical input. For human-motion measurement, independent local-deformation records can provide a reference for identifying strain-transfer errors caused by slip, changes in pretension, or local interfacial peeling.

After deformation reaches the gel, the resulting electrical changes must pass through gel–electrode contacts to the measurement terminals. Electrode interfaces and readout conditions therefore also affect the final signal. Using different strain sequences for the same aqueous gel, Song et al. observed continuous baseline drift with DC resistance readout and a relatively stable baseline with AC impedance readout. The authors associated this difference with interfacial double layers and electrochemical processes under the respective test conditions described in Section 3.2 [63].

Step responses in metal-coordinated gels further demonstrate the joint influence of network composition, electrode contact, and bias. Khodami et al. recorded iron- and copper-coordinated gels using successive 50% strain increments followed by 10 s holds. The copper system showed relatively symmetric loading–unloading steps at 3 V, whereas the iron system showed direction dependence at 0.5 V and drift during most holds. When the iron-system voltage increased to 3 V, the authors observed Faradaic reactions between the gel and aluminum foil and a current decrease to zero. The response differences therefore involve the network, electrode interface, and bias together and cannot be assigned entirely to gel-network recovery [62].

Local structural modification provides a route to improving the metal–gel electrical contact itself. Luo et al. introduced zinc ions near the contact region to create a locally dense structure, increasing adhesion and reducing interfacial impedance. They attributed these changes to mechanical interlocking and formation of local structural junctions. Local densification also provided strain isolation, allowing stable electrode connections to coexist with deformation of the sensing region [99]. Reduced interfacial impedance indicates improved electrical contact, whereas step outputs and sensing loops additionally reflect the combined effects of gel deformation, interfacial processes, and readout. Their interpretation requires the corresponding electrodes, bias, and frequency conditions.

Once a gel is assembled with a protective layer, output also depends on how the layers deform together. Choi et al. encapsulated PVA/borax/multiwalled-carbon-nanotube gels in an acrylic elastomer. Figure 9a–c shows the assembled device's piecewise strain response and repeatable step output. At 25% strain, loading and unloading branches remain separated in Figure 9d, while waveforms from different cycles overlap well in Figure 9e, demonstrating coexistence of loading–unloading hysteresis and cyclic repeatability. Figure 9f compares three independent devices. Figure 9g records output for more than 4000 s at 50% strain and shows waveforms from the beginning and end; the authors report negligible baseline drift. Figure 9h shows that porcine-skin surface conditions affect peel force. Together, these results characterize the assembled device, including its gel, interfaces, and outer layer. Isolating the encapsulation contribution requires comparison with an unencapsulated gel device under identical conditions [9].

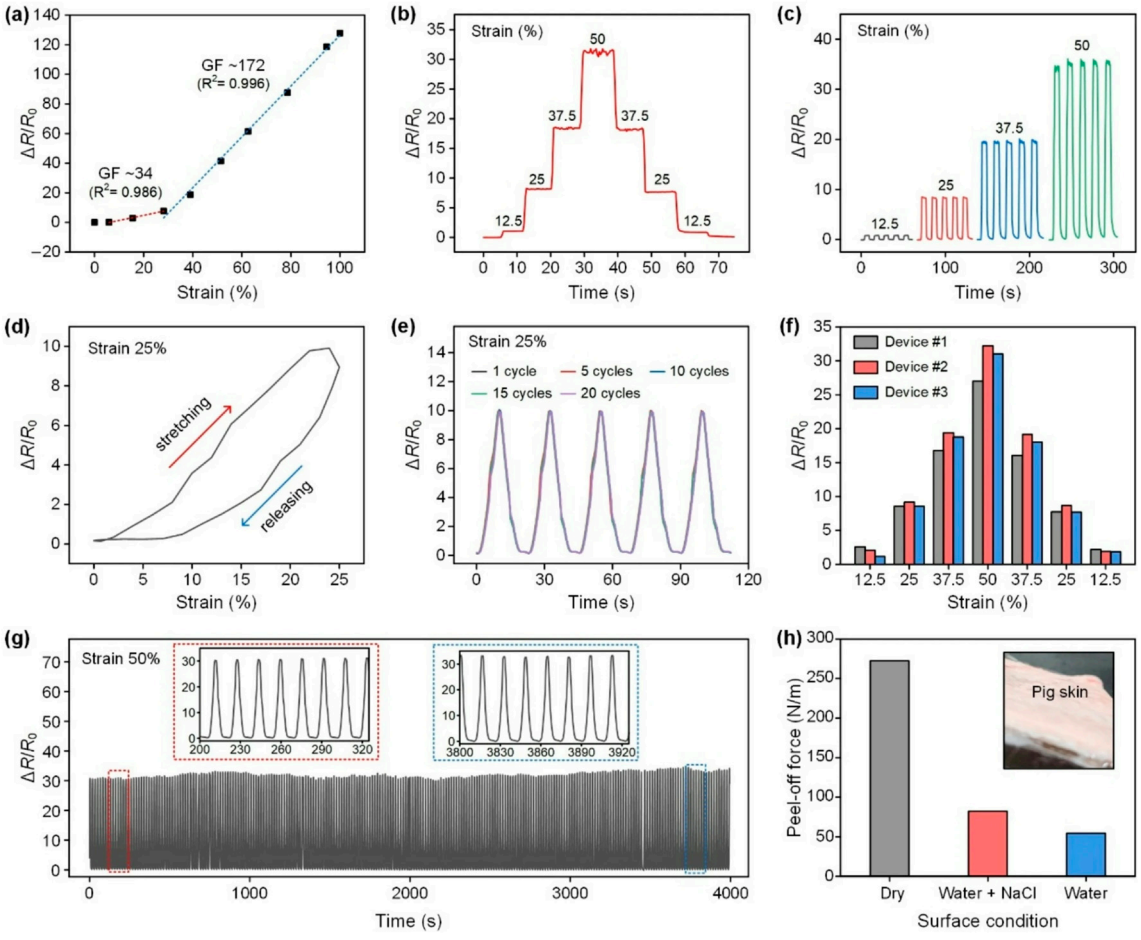



**Figure 9.** Electromechanical performance and stability of the PVA/Borax/MWCNT-hydrogel-based strain sensor. (**a**) Relative resistance change as a function of applied strain from 0% to 100%, showing

two distinct linear regions with GF of 34 and 172 for low- and high-strain regimes, respectively. (**b**) Stepwise response of the sensor under sequential strain levels, demonstrating distinct and stable signal plateaus. (**c**) Dynamic strain-sensing behavior during repetitive step loading, confirming rapid and reversible response over multiple strain amplitudes. (**d**) Loading–unloading curve at 25% strain exhibiting hysteresis due to the viscoelastic nature of the hydrogel and partial rearrangement of the MWCNT network. (**e**) Signal repeatability test under cyclic stretching at 25% strain for 1–20 cycles, showing nearly identical $\Delta R/R_0$. (**f**) Device-to-device consistency evaluated among three independent samples, demonstrating uniform strain-sensing characteristics. (**g**) Long-term cyclic stability under continuous stretching at 50% strain for over 4000 s, with negligible baseline drift; insets show stable waveforms at the beginning and end of the test. (**h**) Adhesion performance of the encapsulated sensor on pig skin under different surface conditions [9].

Protective layers contribute to interlayer load transfer and overall recovery while regulating gel–environment water exchange. Shen et al. combined silicone–rubber protection, interlayer bonding, and internal gel interlocking in one device; its low electrical hysteresis reflects the complete structure [8]. Zhao et al. used thermoplastic–polyurethane interlocking to improve bonding between gel and polydimethylsiloxane, reducing separation through modulus matching and interlayer connections. The working gel contained 30 wt% glycerol. At 28 °C and approximately 30% relative humidity, encapsulated specimens lost approximately 4.6 wt% mass after 24 h and 46% after 21 days. Encapsulation delayed water loss from the water–glycerol system but did not maintain a constant long-term hydration state [100].

Protective layers also influence overall recovery through the constraint imposed by an elastic outer layer on a viscoelastic layer. In composite capacitive devices using water–glycerol gel electrodes, He et al. improved overall elastic recovery by strengthening interfacial connections and using elastic outer layers to constrain a viscoelastic layer [101]. Outer-layer thickness, stiffness, and bonding jointly affect interlayer force transfer. Stronger constraint may promote retraction but can also alter the actual strain in the sensing region. The encapsulated strain–signal relationship therefore depends on joint deformation of the gel and protective layers and cannot be inferred solely from the bare gel's response.

### *4.4. Operating Conditions and Signal Retention*

Prestretching and precycling change the network state during reloading, allowing devices with identical compositions to exhibit different cyclic responses. Cao et al. applied 200% prestretching to a polypyrrole composite-gel framework. Compared with untreated specimens, treated materials showed better loading–unloading agreement within a 100% elastic-deformation range. The authors attributed reduced low-strain dissipation to short-chain rupture during prestretching [85]. Shen et al. used precycling conditioning and conducted 2000 cycles at 100% strain after approximately 300 conditioning cycles. Their reported stable long-term output therefore describes a precycled state and cannot directly represent an initially untreated specimen [8].

The effect of initial loading history also depends on subsequent deformation amplitude. In polyrotaxane networks with movable crosslinks, Huang et al. observed low mechanical hysteresis at 100% strain after the first cycle; dissipation during initial loading differed from that at strain amplitudes of 50–800% [11]. Prestretching effects on crack resistance likewise depend on treatment level. Zheng et al. found that prestretching double-network hydrogels below the yielding region reduced crack resistance, whereas further prestretching beyond that region increased it. They associated these changes with reduced dissipation and release of hidden chain length, respectively [102]. Pretreatment can improve output consistency over a particular working range, but its effects on subsequent cycling and crack resistance must be evaluated in relation to network structure and loading amplitude.

Loading speed also affects the temporal relationship between network deformation and electrical output. Under identical dynamic inputs, Meng et al. compared nanoparticle-crosslinked and conventional polyacrylamide gels. The former retained better current waveforms at a stretch ratio of 3 over 1.2–20 Hz. A separate test with lithium chloride added lasted 200 s at 10 Hz, supporting signal tracking under those short-duration, high-frequency conditions [4]. Cao et al.'s layered hydrogel fibers used capacitive readout at 50% strain over 0.1–2.5 Hz, with response and recovery times of approximately 63 and 62 ms, respectively [5]. The studies differ in strain amplitude and readout signal; their results characterize dynamic responses under their respective conditions and cannot be ranked directly by frequency range or response time.

Network connections and particle structures have also been adjusted to improve tolerance to loading-speed changes. Wu et al. locked highly entangled networks through coordination, producing fibers with response and recovery times both below 40 ms. The authors also reported adaptability to changes in loading rate [89]. Ji et al.'s biomimetic silica-composite gels showed mechanical responses with low rate sensitivity and stability in physiological media. Kim et al.'s in situ mineralized networks demonstrated rate adaptability during cyclic strain sensing [103,104]. These studies use different deformation amplitudes, readout conditions, and metrics. Response time describes input–output timing, whereas waveforms at varying frequencies describe adaptation to changing loading schedules; both must be evaluated separately from signal retention during prolonged cycling.

Moving from controlled stretching to underwater motion monitoring requires devices to tolerate contact with surrounding water. Zhou et al.'s epithelium-like microgel structure connects large-strain response with underwater monitoring. Figure 10 compares the base formulation PLTAV with PLTAV-SC, treated using sorbitol/choline chloride solution. Figure 10a,b shows strain-response slopes and response and recovery times during loading and unloading. Figure 10c,d shows small-strain responses at 3%, 6%, and 9% and large-strain responses at 600%, 900%, and 1200%, respectively, demonstrating response to different deformation amplitudes. Figure 10e records resistance responses at 600% strain and 0.37, 0.67, and 1.67 Hz; Figure 10f shows signal retention during continuous loading–unloading cycles at the same 600% strain. Figure 10g,h addresses compressive-stress response and comparison with existing sensors in linear strain range, self-powered strain sensing, visual strain sensing, and freezing resistance.

Adding hydrophobic layers outside these sensing networks extends PLTAV-H and PLTAV-SC-H devices to underwater monitoring. Figure 10i–l shows underwater finger, wrist, and elbow bending; Figure 10m records wrist pulse; Figure 10n,o shows motion of a water-snake model; and Figure 10p–s addresses water-flow velocity, water-depth detection, and corresponding resistance responses. In these devices, hydrophobic coatings regulate exchange between the sensing body and surrounding water, enabling the monitoring of dynamic deformation during immersion [77].

Environmental exposure changes hydration and ionic-transport conditions, altering the material state underlying dynamic response. Harsh environments may stiffen gels or damage their structures, motivating water-retention and antifreezing designs that preserve the working liquid phase and network state [105,106]. After 4 h at 22 °C and 45% relative humidity, the relative resistance response of Lee et al.'s adhesive gel during finger bending changed from approximately 35% to 60%, which the authors associated with water loss. This demonstrates output changes in a worn device after exposure, but the contributions of hydration and actual local deformation were not separated [60].

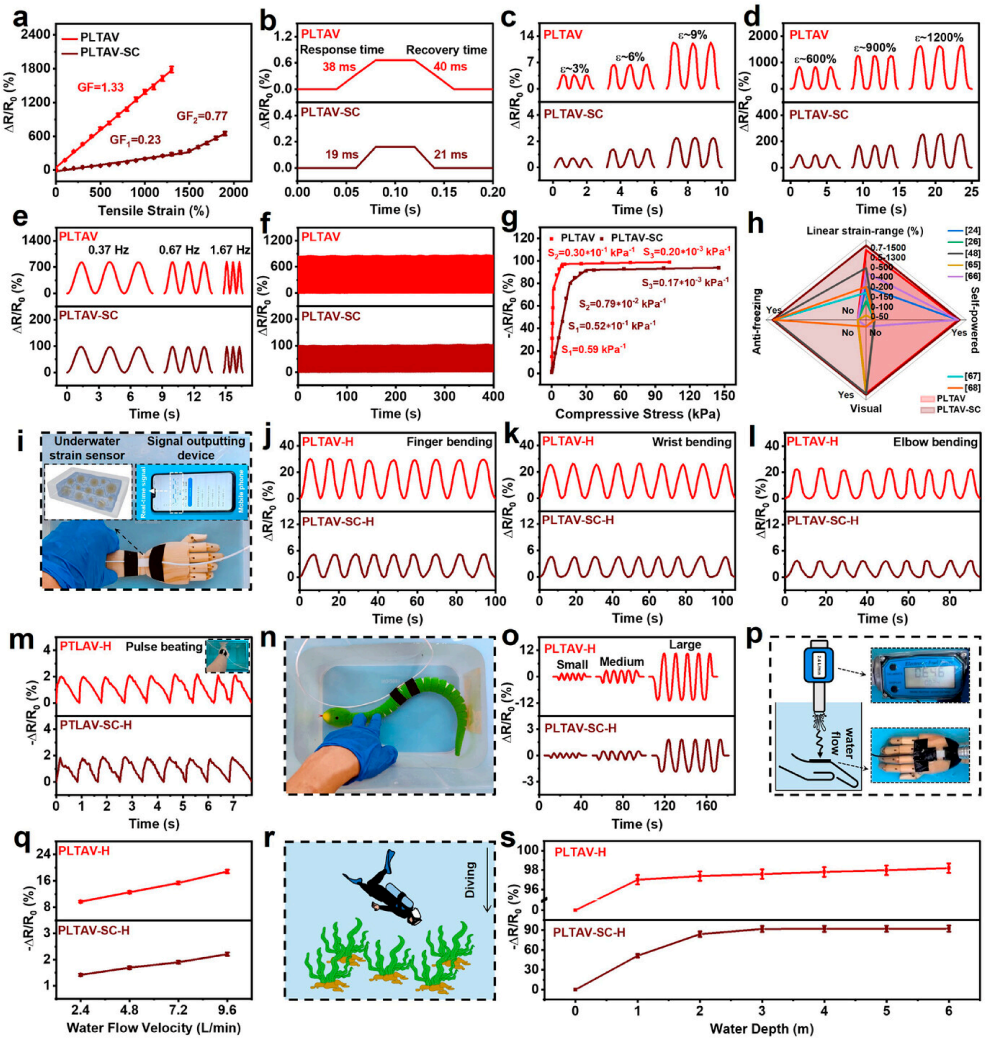



**Figure 10.** Resistance-type sensing properties and potential underwater applications of PLTAV and PLTAV-SC hydrogel strain sensors. (**a**) Relative resistance changes in PLTAV and PLTAV-SC sensors with tensile strain. (**b**) Response and recovery times of PLTAV and PLTAV-SC sensors during loading and unloading. Relative resistance changes in PLTAV and PLTAV-SC sensors at (**c**) minor tensile strains (3%, 6%, and 9%) and (**d**) large tensile strains (600%, 900%, and 1200%). (**e**) Relative resistance changes in PLTAV and PLTAV-SC sensors at a 600% tensile strain under different frequencies. (**f**) Relative resistance changes in PLTAV and PLTAV-SC sensors during loading–unloading cycles at a 600% tensile strain. (**g**) Relative resistance changes in PLTAV and PLTAV-SC sensors with compressive stress. (**h**) Comparison of linear strain range, self-powered strain sensing, visual strain sensing, and anti-freezing abilities of PLTAV and PLTAV-SC strain sensors with previously reported strain sensors. (**i**) PLTAV-H and PLTAV-SC-H sensors for underwater human motion detection. Variation in real-time relative resistance of PLTAV-H and PLTAV-SC-H sensors with (**j**) finger, (**k**) wrist, and (**l**) elbow bending. (**m**) Variation in real-time relative resistance of PLTAV-H and PLTAV-SC-H sensors with wrist pulse beating. (**n**) PLTAV-H and PLTAV-SC-H sensors for underwater animal motion detection. (**o**) Variation in real-time relative resistance of PLTAV-H and PLTAV-SC-H sensors with water snake swinging. (**p**) PLTAV-H and PLTAV-SC-H sensors for water flow velocity detection. (**q**) Variation in relative resistance of PLTAV-H and PLTAV-SC-H sensors with water flow velocity. (**r**) PLTAV-H and PLTAV-SC-H sensors for water depth detection. (**s**) Variation in relative resistance of PLTAV-H and PLTAV-SC-H sensors with water depth [77].

Water retention in air and swelling resistance underwater address changes caused by water loss and uptake, respectively. Zhou et al. combined network crosslinking with equilibration in aqueous calcium chloride and performed mechanical and electrical tests

under specified conditions including 20 °C and 60% relative humidity. They reported low hysteresis and sustained cyclic signals. This strategy jointly regulates water retention, network state, and the ionic environment; performance changes cannot be attributed to water retention alone [57]. Tang et al. instead controlled underwater water uptake and dimensional change through antiswelling design. Their nanocomposite gel completed 3500 cycles at 60% strain underwater, and a separate test measured 3.45% swelling after 60 days of immersion. These independent tests assess cyclic output retention and uptake control after prolonged immersion, respectively [107].

Cosolvent adjustment provides an environmental-adaptation route based on liquid-phase composition. Hardman et al. found that environmental changes still produced substantial baseline-resistance changes in glycerol-modified gelatin, while relative sensitivity remained similar [46]. Wang et al. used a polyacrylamide/carboxymethylcellulose glycerol–water system whose water-retention design supported wireless plant-growth monitoring, demonstrating liquid-phase adjustment for slow-deformation sensing [108]. Water retention, swelling resistance, and cosolvent adjustment can slow material-state changes caused by different environmental exchange processes. Whether the device baseline is maintained still depends on specific operating conditions.

Loading history, motion speed, and environmental exposure may separately alter baseline, response amplitude, and dynamic measurement error. Assessment during sustained use must therefore specify which signal quantity is retained. Amplitude retention and baseline stability should be evaluated separately, and cyclic signal retention cannot be directly equated with strain measurement accuracy [10,96]. When environmental changes shift the baseline while relative sensitivity remains similar, remeasuring the reference value can correct part of the baseline error, as illustrated by Hardman et al. [46].

Sustained cyclic output and dynamic measurement deviation are also different metrics. He et al.'s composite capacitive devices with water–glycerol gel electrodes underwent 10,000 cycles over 18 h at 50% strain, with signal variation of approximately ±2%. Separately, the study defined dynamic-test failure as relative error in the time derivative of strain exceeding 10% [101]. Continuous absolute-strain measurement requires retention of the baseline and strain–signal relationship as well as the response amplitude. Rezeroing can compensate for some baseline shifts but does not automatically remove changes associated with response slope or loading speed; rapid-motion tracking additionally requires consideration of dynamic error. Material and device working ranges should therefore be specified in relation to the measured quantity, loading schedule, and environment.

### *4.5. Damage Suppression and Cyclic Durability*

Crack-resistant design under repeated deformation must combine low energy loss during ordinary loading with local protection near cracks. Guo et al. designed strong metal-coordination connections that remain intact under ordinary loading but rupture and dissipate energy near cracks. Small bulk hysteresis loops can therefore coexist with crack-tip dissipation, providing local crack protection without requiring increased cyclic loss throughout the material [109]. Zheng et al. exploited kinetic differences between two types of metal-coordination connections, allowing stronger connections to rupture preferentially and dissipate energy while protecting weaker reversible connections. This produced a large inelastic zone that distributed crack-tip stress. At an energy release rate of 1000 J/m$^2$, the gel exhibited approximately 1.08 mm of crack growth after one million loading cycles [110]. The two studies, respectively, address how connection states differ between ordinary and crack-tip loading and how the kinetics of different connection types divide their roles. Selective rupture regulates where and how dissipation occurs, allowing repeated load bearing and crack protection to be combined.

Changing local load transfer provides another route to reducing crack-tip stress concentration. Si et al. introduced metal dendrites that shared stress with a dense network and obstructed crack growth. The fatigue threshold reached 720 J/m$^2$, approximately 11 times that of the original gel. Mechanical hysteresis also increased, showing that the gain in crack resistance accompanied greater cyclic energy loss [83]. Chain motion and nanoconfinement offer different stress-regulation mechanisms. Yuan et al. used transiently entangled dangling chains to dissipate energy through sliding and disentanglement and redistribute stress near crack tips [38]. Li et al. conducted confined polymerization within covalent-organic-framework or molecular-sieve channels, using rigid nanostructures to alleviate crack-tip stress concentration. They attributed crack resistance to self-reinforcement arising from hydrogen bonding and channel confinement [111]. Dendrite load sharing, transient chain entanglement, and geometric confinement each alter forces near a crack, demonstrating design routes based on local load distribution and crack paths. Their effects on ordinary cyclic dissipation must still be evaluated under the relevant operating conditions.

Network hydration also affects cyclic load bearing and crack growth. Zhong et al. studied slightly dehydrated, loosely crosslinked hydrogels containing approximately 70 wt% water, evaluating fatigue resistance in a closed environment at 95–100% relative humidity. Figure 11 connects cyclic loading of intact specimens with crack growth in prenotched specimens. Figure 11a,b shows the loading arrangements for notched and unnotched specimens, respectively. At a maximum stretch ratio of 2.65, peak stress in Figure 11c stabilizes after approximately 100 cycles, while Figure 11d shows progressive stabilization of hysteresis loops at different maximum stretch ratios. These results describe the transition from early cyclic adjustment to relatively stable load bearing. Whether crack growth arrests also depends on the applied energy release rate. Figure 11e,f shows crack growth during the first several thousand cycles followed by apparent arrest at 256.1 J/m$^2$, but sustained growth when the energy release rate increases to 425.3 J/m$^2$. From crack growth per cycle versus energy release rate, Figure 11g determines a fatigue threshold of 291.4 J/m$^2$ [112]. Stable peak stress and hysteresis loops describe cyclic load bearing after initial adjustment; crack-growth tests directly examine whether sustained propagation can be prevented under a given load. Together, these tests connect hydration, cyclic load bearing, and crack resistance, informing fatigue-resistant design at relatively high water content.

Crystallization, orientation, and dense interchain structures improve crack resistance by creating relatively stable crack-blocking units. Zhang et al. combined freeze casting and salting-out to form anisotropic conductive gels with fatigue thresholds above 300 J/m$^2$ and used devices for underwater robotic-motion detection, connecting crack-resistant structure with sensing applications [113]. Jia et al. combined crystallization and orientation; notched specimens showed no appreciable crack growth after 2000 stretch–release cycles at 100% strain, demonstrating crack blocking under those conditions [114].

Stronger interchain interactions also depend on hydration and postprocessing. Wu et al. used alcohol-induced gelation and salting-out to strengthen PVA interchain interactions, obtaining a fatigue threshold of approximately 1838 J/m$^2$ at 20.2 wt% water. This illustrates the joint contribution of low hydration and dense interchain connections to crack resistance [115]. Wet annealing provides another reinforcement route, combining macromolecular crystallization and chain entanglements into stable load-bearing units for cyclic crack resistance [79].

Structural reinforcement can also address directional differences in crack resistance. Liang et al. used hierarchical structures to achieve fatigue thresholds above 1500 J/m$^2$ in both in-plane directions, reducing dependence on a single reinforcement direction [80]. Orientation, crystallization, dense interchain connections, and hierarchical organization create persistent barriers to crack growth whose effectiveness depends on their orientation

relative to the crack. Dehydration, orientation, and postprocessing also alter compliance and operating state. Fatigue thresholds must therefore be interpreted with structural direction, hydration, and operating conditions specified and cannot directly establish improved electrical response or longer measurement lifetime.

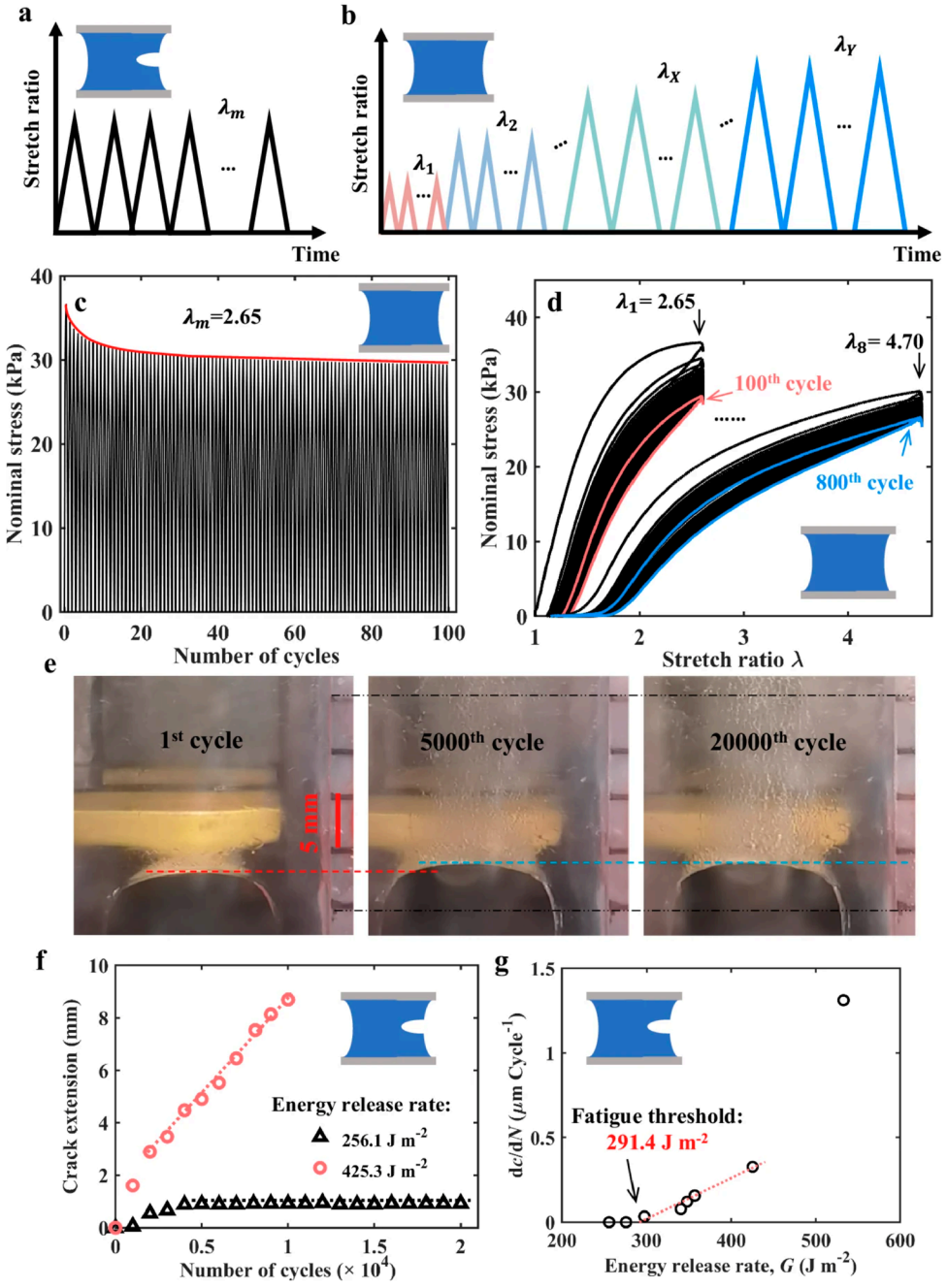



**Figure 11.** Fatigue-resistance of slightly dehydrated LC hydrogels. (**a**) A precut slightly dehydrated LC hydrogel ($\phi_w = 70\%$) is cyclically loaded with a maximal stretch ratio of $\lambda_m$, and the crack growth process is recorded. (**b**) An uncut sample is cyclically loaded with an increasing maximal stretch ratio to measure the corresponding energy release rates. (**c**) With $\lambda_m = 2.65$, the maximal stress of each cycle decays to a stable value after 100 cycles. (**d**) Stable hysteresis loops are observed after 100 cycles with certain $\lambda_m$. (**e**) A precut sample is loaded with an energy release rate of 256.1 J m$^{-2}$. The crack grows during the initial few thousand cycles and then is immobilized. (**f**) The crack growth process of precut samples under various energy release rates. (**g**) The relationship between crack extension per cycle (dc/dN) and the energy release rate (**g**). The calculated fatigue threshold is 291.4 J m$^{-2}$ [112].

Multilayer devices also require protection of connections between gels and elastomers, electrodes, or outer layers to prevent interfacial separation from disrupting the overall structure. Wang et al. used hydrogen-bond-pinned entanglements at hydrogel–elastomer interfaces to alleviate local stress concentration and blunt cracks, achieving interfacial toughness above 1650 J/m$^2$ and an interfacial fatigue threshold of 423 J/m$^2$. These values characterize resistance to interfacial crack propagation under a single loading event and under cyclic loading, respectively, and describe distinct interfacial properties [53].

For gel coatings on metal electrodes, Xue et al. used interfacial nanocrystalline domains to suppress cracking and delamination caused by volume cycling. Lower pacing thresholds and improved electrical-stimulation reliability in cardiac pacing linked interfacial protection to actual electrical function [54]. Yuan et al. introduced textiles into gel coatings, transferring part of the load to fibers and expanding the loaded region, while a wrinkled interface altered crack paths. The interfacial fatigue threshold was approximately eight times that of the control [116]. Hydrogen-bond pinning, interfacial crystalline reinforcement, and textile load distribution suppress cyclic damage under concentrated interfacial loading through different routes. Multilayer durability therefore requires both bulk crack resistance and sustained interfacial load transfer and connectivity. For strain sensing, continued deformation transfer and conductive contact must also be examined; interfacial toughness or adhesion strength from a single loading event does not establish long-term measurement reliability.

Electrical tests with defects further assess whether crack-resistant structures support continued device operation. Si et al. applied 50% strain to notched and unnotched devices and observed no appreciable attenuation after 200 resistance cycles, demonstrating short-term repeatable output under specified defect conditions [83]. Shi et al.'s repaired gels retained slight drift during cycling at 50% and 100% strain, while repeated loading at 200% strain produced cracks and increased response amplitude. Structural damage and signal changes caused by large deformation may therefore persist after conductive pathways resume operation [68].

Joint mechanical and electrical records help establish correspondence between load-bearing states and output changes. Zhang et al. concurrently recorded relative force and resistance in three-dimensionally printed, microphase-interlocked devices over 10,000 cycles at 100% strain and 500 mm/min. They reported negligible drift and retention of mechanical state and electrical output, providing more direct evidence for comparing mechanical and electrical behavior under the same loading conditions [93]. Jia et al. reported structural retention and resistive strain response in separate crack-resistance and sensing experiments, respectively [114].

Postcycling damage observations directly support structural retention. Zhang et al.'s PVA/silver-nanowire gels showed no appreciable microcracks after 5000 mechanical cycles at 65% strain, indicating integrity under the specified conditions and observation scale. Retention of electrical calibration still requires corresponding validation [117]. Sheng et al. observed no appreciable surface cracks after 400 cycles at 500% strain. A separate test showed retained electrical-signal transmission after 1000 cycles. The two separate tests support surface integrity and retained electrical-signal transmission under their respective cycling conditions [118]. Defect tolerance and structural retention underpin repeated operation, but determining whether damage affects measurement requires links among crack formation, local deformation, relative force, and electrical output.

Long-duration electrical cycling further examines output retention. Cao et al.'s layered fibers completed 10,000 capacitance cycles at 200% strain without appreciable baseline drift, demonstrating retention of capacitance output during cycling under those conditions [5]. Huang et al.'s polyrotaxane devices maintained stable electrical output after 10,000 cycles at 20% strain [11]. Zhang et al.'s anisotropic gel devices also retained signals for more

than 10,000 cycles, linking crack-resistant structure with sustained sensing output [113]. These results demonstrate durability advances, but completing 10,000 cycles at different strain amplitudes, with different structures and readout modes, does not establish the same measurement lifetime.

Measurement lifetime additionally requires task-specific failure endpoints. In dynamic measurements with composite capacitive devices using water–glycerol gel electrodes, He et al. defined failure in a particular test as relative strain-rate error exceeding 10%, separately evaluating cyclic output retention and dynamic measurement deviation [101]. Practical tasks require specified allowable error, loading speed, environment, and failure endpoint. Continued usability depends on retention of load-bearing structures, conductive connections, and the strain–signal relationship under target conditions, not solely on whether cracks propagate. Where appropriate, recovery during rest, rehydration, and recalibration should also be evaluated as operating and maintenance conditions. Examining crack resistance, low hysteresis, and cyclic reliability under common conditions is necessary to determine sustained strain-measurement capability.

## 5. Challenges and Conclusions

Cyclic reliability of conductive hydrogel strain sensors depends on whether load-bearing networks, conductive pathways, and device interfaces jointly maintain the required strain–signal relationship during repeated deformation. Movable connections, controlled entanglements, reversible ordering, and microphase interlocking offer distinct routes to improved structural recovery and repeatable output [5,8,11]. The ability to withstand repeated deformation underpins sustained operation, but stable measurement output must also be evaluated against actual loading schedules, recovery times, and environments. Mechanical dissipation, electrical hysteresis, and calibration retention should therefore be assessed separately before determining whether they jointly meet the requirements of a specific measurement task.

Recovery timescales connect structural design with actual measurement schedules. Modulus, peak stress, and dissipated energy may recover to different extents over the same rest period, reflecting differences in the recovery of individual mechanical responses [7]. A single mechanical metric may therefore be insufficient to predict performance under continuous loading. Continuous measurement requires network recovery compatible with the loading schedule, whereas intermittent measurement can use pauses to rebuild reversible structures. Future work can address this distinction by tuning formation and rupture kinetics of reversible connections or changing chain constraints, while jointly recording structural, mechanical, and electrical changes across loading rates and rest intervals. Comparisons should match water content, geometry, and initial mechanical response as closely as possible to distinguish structural-design effects from initial material-state effects. This would identify recovery processes that limit continuous tracking and establish whether adjusting recovery rates expands the operating range over which the original calibration remains valid.

The relationship between load-bearing network recovery and conductive-pathway recovery requires joint mechanical and electrical assessment. Existing studies show that baseline drift can persist despite stable amplitude and waveform, and electrical hysteresis can remain despite repeatable outputs across cycles [9,10]. Neither mechanical recovery nor repeatable waveforms alone establish retention of the original strain calibration. Future comparisons of microphase interlocking, spatial separation, and layered structures could record local strain, stress, and electrical signals together under identical mechanical inputs, examining changes in load-bearing networks and conductive pathways while accounting for resistive, capacitive, and other readout mechanisms. Such comparisons would help separate

the effects of deformation transfer and charge transport on readout and determine whether baseline, response slope, and loading–unloading relationships jointly meet predefined error limits across the target range.

Hydration and interfacial connections jointly affect the measurement performance of an assembled device after environmental exposure. Protective layers regulate water exchange while influencing deformation transfer and mechanical constraint; electrode contact and electrical excitation also affect readout. Improvements in water retention and adhesion should therefore be evaluated alongside actual measurement performance. Future studies could compare protection and bonding strategies at fixed liquid-phase composition and readout conditions, jointly tracking hydration, local strain, contact stability, and electrical output during environmental changes. Measurement before and after rehydration and reference-value correction should also be assessed separately to identify the contribution of each maintenance action and changes that remain uncompensated. Extending results from organic-cosolvent-containing hydrogels to predominantly aqueous systems requires verification of how liquid-phase composition affects network structure, interfacial connections, and electrical transport.

Extending measurement lifetime requires connecting structural-damage evolution with measurement failure. Local dissipation and crack barriers can protect material structure, but some reinforcement methods also increase mechanical hysteresis; crack-resistance gains should therefore be considered alongside energy loss during ordinary cycling [83,109]. Future work could compare intact devices with devices containing controlled initial defects under common loading conditions, continuously recording crack growth, interfacial separation, and calibration error. This would establish when structural protection delays measurement failure and which defects devices can tolerate. Measurement failure should be defined by error exceeding task limits and distinguished from structural fracture: a device may lose the required measurement capability through baseline shifts or changes in the strain–signal relationship before appreciable cracks appear. Reports should distinguish the duration of a completed test from the lifetime determined by an observed failure, avoiding claims that passing a prescribed cycle count proves long-term service life.

Several chemistries offer promising routes when matched to specific device requirements. PVA/PEDOT:PSS composites couple a compliant framework to an interconnected electronic phase for resistive motion sensing [8]. Charged copolymer networks provide adaptable ionic conductors in which reversible interactions and ion distribution can be tuned together [18,60]. Layered sodium polyacrylate hydrogel fibers offer a route to capacitive sensing by combining deformable layers with interfacial charge storage [5]. Their practical advantages should be assessed at the intended loading schedule: continuous tracking requires sufficiently rapid mechanical and electrical recovery, whereas extended exposure to air or water requires separate control of water loss or uptake. Material selection should be guided by the intended application and account for conductive pathways, encapsulation, and calibration retention across devices.

Future research can begin with a specific measurement task, identify the process limiting reliability, modify it through structural design, and then test the improvement across independent devices, preparation batches, and repeated mounting. Structural recovery, charge transport, and damage tolerance should be designed together around the same measurement requirement. Only when these structures and processes jointly retain the strain–signal relationship at specified loading amplitudes, speeds, and environmental conditions can material innovations reliably support repeated-motion monitoring and feedback for soft robots.

**Author Contributions:** Conceptualization, J.D. and S.H.; methodology, J.D.; validation, J.D.; data curation, J.D.; writing—original draft preparation, J.D.; writing—review and editing, J.D. and S.H.; supervision, S.H.; project administration, S.H. All authors have read and agreed to the published version of the manuscript.

**Funding:** This research received no external funding.

**Institutional Review Board Statement:** Not applicable.

**Informed Consent Statement:** Not applicable.

**Data Availability Statement:** No new data were created or analyzed in this study. Data sharing is not applicable to this article.

**Conflicts of Interest:** The authors declare no conflicts of interest.

## References

1. Roy, A.; Afshari, R.; Jain, S.; Zheng, Y.; Lin, M.-H.; Zenkar, S.; Yin, J.; Chen, J.; Peppas, N.A.; Annabi, N. Advances in conducting nanocomposite hydrogels for wearable biomonitoring. *Chem. Soc. Rev.* **2025**, *54*, 2595–2652. [CrossRef] [PubMed]
2. Lee, M.Y.; Lee, E.S.; Ko, N.Y.; Kim, H.J.; Kim, D.-H.; Cha, G.D.; Koo, J.H. Emerging roles of hydrogels, organogels, and their hybrids in soft bioelectronics and bioplatforms. *npj Biosens.* **2025**, *2*, 35. [CrossRef]
3. Li, G.; Li, C.; Li, G.; Yu, D.; Song, Z.; Wang, H.; Liu, X.; Liu, H.; Liu, W. Development of Conductive Hydrogels for Fabricating Flexible Strain Sensors. *Small* **2022**, *18*, 2101518. [CrossRef] [PubMed]
4. Meng, X.; Qiao, Y.; Do, C.; Bras, W.; He, C.; Ke, Y.; Russell, T.P.; Qiu, D. Hysteresis-Free Nanoparticle-Reinforced Hydrogels. *Adv. Mater.* **2022**, *34*, 2108243. [CrossRef] [PubMed]
5. Cao, P.; Wang, Y.; Yang, J.; Niu, S.; Pan, X.; Lu, W.; Li, L.; Xu, Y.; Cui, J.; Ho, G.W.; et al. Scalable Layered Heterogeneous Hydrogel Fibers with Strain-Induced Crystallization for Tough, Resilient, and Highly Conductive Soft Bioelectronics. *Adv. Mater.* **2024**, *36*, 2409632. [CrossRef] [PubMed]
6. Di Pasquale, G.; Pollicino, A. Conductive Hydrogels for Wearable Sensing: Materials, Mechanics, and Multimodal Interfaces. *Appl. Sci.* **2026**, *16*, 7546. [CrossRef]
7. Huang, Y.-X.; Luo, M.-D.; Ye, D.; Li, J.; Shu, K.; Chen, X.-P.; Zheng, K. Mechanically robust and rapidly self-recovering hyaluronic acid-based conductive hydrogels via fully physical double-network crosslinking for sensitive strain sensors. *Chem. Eng. J.* **2025**, *525*, 170488. [CrossRef]
8. Shen, Z.; Zhang, Z.; Zhang, N.; Li, J.; Zhou, P.; Hu, F.; Rong, Y.; Lu, B.; Gu, G. High-Stretchability, Ultralow-Hysteresis ConductingPolymer Hydrogel Strain Sensors for Soft Machines. *Adv. Mater.* **2022**, *34*, 2203650. [CrossRef] [PubMed]
9. Choi, J.-A.; Kang, M.; Jeong, J.; Pyo, S. A highly sensitive and stretchable PVA-based hydrogel strain sensor with facile acrylic elastomer encapsulation. *Micro Nano Syst. Lett.* **2025**, *13*, 20. [CrossRef]
10. Han, Q.; Li, M.; Liu, C.; Qu, Y.; Li, S.; Guan, S. A multifunctional anti-swelling hydrogel with high stretchability and adhesion for wearable flexible sensors. *J. Mater. Chem. C Mater.* **2026**, *14*, 372–384. [CrossRef]
11. Huang, H.-Z.; Zheng, Y.-T.; Chen, F.; Li, J.-Y.; Zhang, W.-H.; Ding, L.; Huang, Z.; Jiang, W.; Huang, L.-P.; Shen, X.-C. A Stretchable, Mechanically-Interlocked Polyrotaxane Hydrogel for Wearable Motion and Electrophysiological Monitoring. *Adv. Sci.* **2026**, *13*, e75205. [CrossRef] [PubMed]
12. Liu, F.-X.; Jing, X.; Yang, J.; Mi, H.-Y.; Feng, F.-Y.; Liu, Y.-J. Recent progress in low hysteresis gels: Strategies, applications, and challenges. *Nano Today* **2025**, *61*, 102601. [CrossRef]
13. Han, S.; Xing, L.; Qin, Y.; Pan, C. Designing resilient hydrogels: Strategies for minimizing hysteresis while maximizing toughness. *Matter* **2026**, *9*, 102489. [CrossRef]
14. Fan, Z.; Ji, D.; Kim, J. Recent Progress in Mechanically Robust and Conductive-Hydrogel-Based Sensors. *Adv. Intell. Syst.* **2023**, *5*, 2300194. [CrossRef]
15. Khan, B.; Khalid, T.; Hilal, M.E.; Hassan, M.; Khan, B.; Shokurov, A.V.; Menon, C.; Elgendi, M.; Khoo, B.L. Emerging trends in conductive PVA hydrogels for wearable personalised health monitoring. *Prog. Mater. Sci.* **2027**, *163*, 101769. [CrossRef]
16. Patel, D.K.; Cha, J.; Han, S.S. Polysaccharide-based hydrogel strain sensors: Materials design, sensing mechanisms, applications, and challenges. *Carbohydr. Polym.* **2026**, *390*, 125792. [CrossRef] [PubMed]
17. Li, Z.; Wu, L.; Rossiter, J. Stretchable and conductive PAAm@PPy hydrogels with low hysteresis for strain sensing. *Interface Focus* **2026**, *16*, 20250049. [CrossRef]
18. Ghosh, A.; Kumar, S.; Singh, P.P.; Nandi, S.; Mandal, M.; Pradhan, D.; Khatua, B.B.; Das, R.K. Dynamic Metal-Coordinated Adhesive and Self-Healable Antifreezing Hydrogels for Strain Sensing, Flexible Supercapacitors, and EMI Shielding Applications. *ACS Omega* **2024**, *9*, 33204–33223. [CrossRef] [PubMed]

19. Sun, T.L.; Kurokawa, T.; Kuroda, S.; Bin Ihsan, A.; Akasaki, T.; Sato, K.; Haque, M.A.; Nakajima, T.; Gong, J.P. Physical hydrogels composed of polyampholytes demonstrate high toughness and viscoelasticity. *Nat. Mater.* **2013**, *12*, 932–937. [CrossRef] [PubMed]
20. Kim, J.; Zhang, G.; Shi, M.; Suo, Z. Fracture, fatigue, and friction of polymers in which entanglements greatly outnumber cross-links. *Science* **2021**, *374*, 212–216. [CrossRef] [PubMed]
21. Ansart, É.; Cousin, L.; Tibbitt, M.W.; Mommer, S. Enhanced toughness in highly entangled hydrogels via non-covalent molecular hooks. *Mater. Horiz.* **2026**, *13*, 940–947. [CrossRef] [PubMed]
22. Gong, J.P.; Katsuyama, Y.; Kurokawa, T.; Osada, Y. Double-Network Hydrogels with Extremely High Mechanical Strength. *Adv. Mater.* **2003**, *15*, 1155–1158. [CrossRef]
23. Sun, J.-Y.; Zhao, X.; Illeperuma, W.R.K.; Chaudhuri, O.; Oh, K.H.; Mooney, D.J.; Vlassak, J.J.; Suo, Z. Highly stretchable and tough hydrogels. *Nature* **2012**, *489*, 133–136. [CrossRef] [PubMed]
24. Irvine, G.; Myronidis, K.; Pinto, F.; Kopeć, M. Highly Entangled Hydrogels by Photoiniferter-Mediated Polymerization. *Angew. Chem. Int. Ed. Engl.* **2025**, *64*, e202421970. [CrossRef] [PubMed]
25. Mandal, S.; Assadi, S.; Visal, A.M.; Lorente Montero, I.; Vernerey, F.J.; Bruns, C.J. Synergistic Dual Slip-Link Toughening of a Water-Rich Double Network Hydrogel Combining Slide-Ring and Highly Entangled Networks. *Adv. Sci.* **2026**, *13*, e75525. [CrossRef] [PubMed]
26. Zhang, Y.; Lou, H.; Yan, C.; Zhang, Q.; Wang, Y.; Zhang, Y. High Entanglement in Hydrogels: From Polymer Physics to Robust Mechanics. *Polym. Sci. Technol.* **2026**, *2*, 222–247. [CrossRef] [PubMed]
27. Ho, T.-C.; Chang, C.-C.; Chan, H.-P.; Chung, T.-W.; Shu, C.-W.; Chuang, K.-P.; Duh, T.-H.; Yang, M.-H.; Tyan, Y.-C. Hydrogels: Properties and Applications in Biomedicine. *Molecules* **2022**, *27*, 2902. [CrossRef] [PubMed]
28. Zhang, G.; Steck, J.; Kim, J.; Ahn, C.H.; Suo, Z. Hydrogels of arrested phase separation simultaneously achieve high strength and low hysteresis. *Sci. Adv.* **2023**, *9*, eadh7742. [CrossRef] [PubMed]
29. Shao, Y.; Ma, Y.; Shao, B.; Stevens, M.M. Harnessing Phase Separation for the Development of High-Performance Hydrogels. *Adv. Sci.* **2026**, e00032. [CrossRef] [PubMed]
30. Li, X.; Gong, J.P. Design principles for strong and tough hydrogels. *Nat. Rev. Mater.* **2024**, *9*, 380–398. [CrossRef]
31. Lu, H.; Yang, Z.; Bai, J.; Ma, Y.; Chen, X.; Yan, L. Dehydration-Induced Chain Entanglement for Tough, Low-Hysteresis, Double-Network Hydrogels. *ACS Appl. Mater. Interfaces* **2026**, *18*, 22512–22522. [CrossRef] [PubMed]
32. Liu, C.; Morimoto, N.; Jiang, L.; Kawahara, S.; Noritomi, T.; Yokoyama, H.; Mayumi, K.; Ito, K. Tough hydrogels with rapid self-reinforcement. *Science* **2021**, *372*, 1078–1081. [CrossRef] [PubMed]
33. Petelinšek, N.; Mommer, S. Tough Hydrogels for Load-Bearing Applications. *Adv. Sci.* **2024**, *11*, 2307404. [CrossRef] [PubMed]
34. Fang, Y.; Bai, Z.; Xu, W.; Xiong, X.; Wei, J.; Hu, Q.; Wang, H.; Cui, J. Mechanical Design Principles of Conductive Gels Applied for Flexible Electronics. *Adv. Funct. Mater.* **2025**, *35*, 2416398. [CrossRef]
35. Zhu, R.; Zhu, D.; Zheng, Z.; Wang, X. Tough double network hydrogels with rapid self-reinforcement and low hysteresis based on highly entangled networks. *Nat. Commun.* **2024**, *15*, 1344. [CrossRef] [PubMed]
36. Ji, F.; Shang, P.; Lai, Y.; Wang, J.; Zhang, G.; Lin, D.; Xu, J.; Cai, D.; Qin, Z. Fully Physically Crosslinked Conductive Hydrogel with Ultrastretchability, Transparency, and Self-Healing Properties for Strain Sensors. *Materials* **2023**, *16*, 6491. [CrossRef] [PubMed]
37. Li, X.; Gong, J.P. Role of dynamic bonds on fatigue threshold of tough hydrogels. *Proc. Natl. Acad. Sci. USA* **2022**, *119*, e2200678119. [CrossRef] [PubMed]
38. Yuan, Z.; Cao, Z.; Wang, H.; Wu, H.; Zheng, J.; Zhang, R.; Wu, J. Tough hydrogels enabled by transient entanglements. *Nat. Commun.* **2026**, *17*, 4145. [CrossRef] [PubMed]
39. Bertsch, P.; Sacco, P. The role of non-linear viscoelastic hydrogel mechanics in cell culture and transduction. *Mater. Today Bio* **2025**, *34*, 102188. [CrossRef] [PubMed]
40. Tanaka, T.; Fillmore, D.J. Kinetics of swelling of gels. *J. Chem. Phys.* **1979**, *70*, 1214–1218. [CrossRef]
41. Di, X.; Hou, J.; Yang, M.; Wu, G.; Sun, P. A bio-inspired, ultra-tough, high-sensitivity, and anti-swelling conductive hydrogel strain sensor for motion detection and information transmission. *Mater. Horiz.* **2022**, *9*, 3057–3069. [CrossRef] [PubMed]
42. Wang, C.; Ding, H.; Deng, Y.; Zhang, L.; Zhai, R.; Li, H.; Zheng, S.Y. An ultra-stretchable, tough yet resilient hydrogel with high fatigue fracture threshold. *Chem. Eng. J.* **2026**, *538*, 176944. [CrossRef]
43. Yan, Y.; Yu, L.; Zhang, X.; Han, Q.; Yang, Z.; Lu, X.; Wang, J.; Xu, H.; Chen, Q.; Zhao, H. Instantaneous self-recovery and ultra-low detection limit hydrogel electronic sensor for temporomandibular disorders intelligent diagnosis. *Nat. Commun.* **2025**, *16*, 839. [CrossRef] [PubMed]
44. Lin, S.; Liu, J.; Liu, X.; Zhao, X. Muscle-like fatigue-resistant hydrogels by mechanical training. *Proc. Natl. Acad. Sci. USA* **2019**, *116*, 10244–10249. [CrossRef] [PubMed]
45. Wang, J.; Li, X.; Liu, Y. Physically Entangled Hydrogels Constructed Through Pre-Stretched Backbone Provide Excellent Comprehensive Mechanical Properties. *Small* **2025**, *21*, 2501666. [CrossRef] [PubMed]
46. Hardman, D.; Thuruthel, T.G.; Iida, F. Self-healing ionic gelatin/glycerol hydrogels for strain sensing applications. *NPG Asia Mater.* **2022**, *14*, 11. [CrossRef]

47. Rivlin, R.S.; Thomas, A.G. Rupture of rubber. I. Characteristic energy for tearing. *J. Polym. Sci.* **1953**, *10*, 291–318. [CrossRef]
48. Wang, Z.; Xiang, C.; Yao, X.; Le Floch, P.; Mendez, J.; Suo, Z. Stretchable materials of high toughness and low hysteresis. *Proc. Natl. Acad. Sci. USA* **2019**, *116*, 5967–5972. [CrossRef] [PubMed]
49. Li, L.; Lei, H.; Cao, Y. Fatigue-resistant Hydrogels. *Chem. Res. Chin. Univ.* **2024**, *40*, 64–77. [CrossRef]
50. Lake, G.J.; Thomas, A.G. The strength of highly elastic materials. *Proc. R. Soc. Lond. A Math. Phys. Sci.* **1967**, *300*, 108–119. [CrossRef]
51. Lin, S.; Liu, X.; Liu, J.; Yuk, H.; Loh, H.-C.; Parada, G.A.; Settens, C.; Song, J.; Masic, A.; McKinley, G.H.; et al. Anti-fatigue-fracture hydrogels. *Sci. Adv.* **2019**, *5*, eaau8528. [CrossRef] [PubMed]
52. Gao, S.; Jiang, L. Analysis of Fatigue Crack Nucleation in Double-Network Hydrogels. *Polymers* **2024**, *16*, 1700. [CrossRef] [PubMed]
53. Wang, Z.; Yang, F.; Liu, X.; Han, X.; Li, X.; Huyan, C.; Liu, D.; Chen, F. Hydrogen Bonds-Pinned Entanglement Blunting the Interfacial Crack of Hydrogel–Elastomer Hybrids. *Adv. Mater.* **2024**, *36*, 2313177. [CrossRef] [PubMed]
54. Xue, Y.; Chen, X.; Wang, F.; Lin, J.; Liu, J. Mechanically-Compliant Bioelectronic Interfaces through Fatigue-Resistant Conducting Polymer Hydrogel Coating. *Adv. Mater.* **2023**, *35*, 2304095. [CrossRef] [PubMed]
55. He, Q.; Cheng, Y.; Deng, Y.; Wen, F.; Lai, Y.; Li, H. Conductive Hydrogel for Flexible Bioelectronic Device: Current Progress and Future Perspective. *Adv. Funct. Mater.* **2024**, *34*, 2308974. [CrossRef]
56. Bi, D.; Qu, N.; Sheng, W.; Lin, T.; Huang, S.; Wang, L.; Li, R. Tough and Strain-Sensitive Organohydrogels Based on MXene and PEDOT/PSS and Their Effects on Mechanical Properties and Strain-Sensing Performance. *ACS Appl. Mater. Interfaces* **2024**, *16*, 11914–11929. [CrossRef] [PubMed]
57. Zhou, L.; Zhao, B.; Liang, J.; Lu, F.; Yang, W.; Xu, J.; Zheng, J.; Liu, Y.; Wang, R.; Liu, Z. Low hysteresis, water retention, anti-freeze multifunctional hydrogel strain sensor for human–machine interfacing and real-time sign language translation. *Mater. Horiz.* **2024**, *11*, 3856–3866. [CrossRef] [PubMed]
58. Zhang, D.; Sun, H.; Huang, M.; Su, M.; Ma, Y.; Shi, M.; Mi, L.; Liu, C.; Liu, H. Construction of "island-bridge" microstructured conductive coating for enhanced impedance response of organohydrogel strain sensor. *Chem. Eng. J.* **2024**, *496*, 153752. [CrossRef]
59. Keplinger, C.; Sun, J.-Y.; Foo, C.C.; Rothemund, P.; Whitesides, G.M.; Suo, Z. Stretchable, Transparent, Ionic Conductors. *Science* **2013**, *341*, 984–987. [CrossRef] [PubMed]
60. Lee, G.; Seo, H.; Kim, D.; Shin, S.; Kwon, K. All polymeric conductive strain sensors with excellent skin adhesion, recovery, and long-term stability prepared from an anion–zwitterion based hydrogel. *RSC Adv.* **2023**, *13*, 1672–1683. [CrossRef] [PubMed]
61. Zhao, Y.; Cui, J.; Qiu, X.; Yan, Y.; Zhang, Z.; Fang, K.; Yang, Y.; Zhang, X.; Huang, J. Manufacturing and post-engineering strategies of hydrogel actuators and sensors: From materials to interfaces. *Adv. Colloid Interface Sci.* **2022**, *308*, 102749. [CrossRef] [PubMed]
62. Khodami, S.; Kaniewska, K.; Romanski, J.; Karbarz, M.; Stojek, Z. Amino Acid-Based Hydrogel with Interpenetrating Gelatin and Cross-Linked by Metal Ions, Providing High Stretchability and Motion Sensitivity. *ACS Omega* **2025**, *10*, 12062–12075. [CrossRef] [PubMed]
63. Song, J.; Mou, C.; Balakrishnan, G.; Wang, Y.; Rajagopalan, M.; Schreiner, A.; Naik, D.; Cohen-Karni, T.; Halbreiner, M.S.; Bettinger, C.J. Hysteresis-Free and High-Sensitivity Strain Sensing of Ionically Conductive Hydrogels. *Adv. Nanobiomed Res.* **2023**, *3*, 2200132. [CrossRef] [PubMed]
64. Saeed, A.; Alam Zaidi, S.F.; Park, C.G.; Lee, J.H. Enhancing Multifunctionality and Performance Indicators of Resistive-Type Strain Sensors with Advanced Conductive Hydrogels. *Adv. Mater. Technol.* **2024**, *9*, 2400355. [CrossRef]
65. Jansen, K.M.B. Performance Evaluation of Knitted and Stitched Textile Strain Sensors. *Sensors* **2020**, *20*, 7236. [CrossRef] [PubMed]
66. Sembiring, Y.S.B.; Vo, T.T.; Entifar, S.A.N.; Wibowo, A.F.; Kim, J.H.; Entifar, N.A.E.; Lee, J.H.; Baek, S.W.; Lee, S.I.; Kim, M.S.; et al. Recyclable, conductive alginate-based hydrogels with high stretchability and low electrical hysteresis for wireless wearable sensors. *J. Mater. Chem. A Mater.* **2025**, *13*, 15200–15212. [CrossRef]
67. Ko, S.; Chhetry, A.; Kim, D.; Yoon, H.; Park, J.Y. Hysteresis-Free Double-Network Hydrogel-Based Strain Sensor for Wearable Smart Bioelectronics. *ACS Appl. Mater. Interfaces* **2022**, *14*, 31363–31372. [CrossRef] [PubMed]
68. Shi, W.; Li, H.; Chen, J.; Ching, Y.C.; Chuah, C.H.; Xu, C.; Liu, M.; Zhang, J.; Ching, K.Y.; Liang, Y.; et al. Stretchable, Self-Healing, and Bioactive Hydrogel with High-Functionality N,N′-bis(acryloyl)cystamine Dynamically Bonded Ag@polydopamine Crosslinkers for Wearable Sensors. *Adv. Sci.* **2024**, *11*, 2404451. [CrossRef] [PubMed]
69. Wu, S.; Tang, L.; Xu, Y.; Yao, J.; Tang, G.; Dai, B.; Wang, W.; Tang, J.; Gong, L. A self-powered flexible sensing system based on a super-tough, high ionic conductivity supercapacitor and a rapid self-recovering fully physically crosslinked double network hydrogel. *J. Mater. Chem. C Mater.* **2022**, *10*, 3027–3035. [CrossRef]
70. Liang, Q.; Xia, X.; Sun, X.; Yu, D.; Huang, X.; Han, G.; Mugo, S.M.; Chen, W.; Zhang, Q. Highly Stretchable Hydrogels as Wearable and Implantable Sensors for Recording Physiological and Brain Neural Signals. *Adv. Sci.* **2022**, *9*, 2201059. [CrossRef] [PubMed]

71. Sun, X.; Luo, F.; Jiang, F. Low-Hysteresis Cellulose-Based Hydrogels for Strain Detecting. *Macromol. Rapid Commun.* **2025**, e00521. [CrossRef] [PubMed]
72. Xiong, X.; Chen, Y.; Wang, Z.; Liu, H.; Le, M.; Lin, C.; Wu, G.; Wang, L.; Shi, X.; Jia, Y.-G.; et al. Polymerizable rotaxane hydrogels for three-dimensional printing fabrication of wearable sensors. *Nat. Commun.* **2023**, *14*, 1331. [CrossRef] [PubMed]
73. Zou, J.; Jing, X.; Li, S.; Feng, P.; Chen, Y.; Liu, Y. MXene Crosslinked Hydrogels with Low Hysteresis Conferred by Sliding Tangle Island Strategy. *Small* **2024**, *20*, e2401622. [CrossRef] [PubMed]
74. Liu, F.; Jing, X.; Li, S.; Xu, Y.; Feng, P.; Mi, H.-Y.; Liu, Y.; Geng, L. Topological entanglement engineering enables anti-fatigue and ultra-Stretchable hydrogels for high-fidelity sensing. *Compos. B Eng.* **2026**, *311*, 113224. [CrossRef]
75. Wang, J.; Tang, F.; Yao, C.; Li, L. Low Hysteresis Hydrogel Induced by Spatial Confinement. *Adv. Funct. Mater.* **2023**, *33*, 2214935. [CrossRef]
76. Wang, S.; Yu, Z.; Sun, X.; Panahi-Sarmad, M.; Yang, P.; Zhu, P.; Zhu, Y.; Liu, H.; Jiang, F. A Universal Strategy to Mitigate Microphase Separation via Cellulose Nanocrystal Hydration in Fabricating Strong, Tough, and Fatigue-Resistant Hydrogels. *Adv. Mater.* **2025**, *37*, 2416916. [CrossRef] [PubMed]
77. Zhou, Y.; Shu, H.; Yao, Y.; Lu, B.; Zhong, W. Epithelium-Inspired, Ultrahigh-Toughness, Ultralow-Hysteresis, and Highly Compressible Polymer Hydrogels as Self-Powered, Visual, and Underwater Strain Sensors. *Adv. Sci.* **2026**, *13*, e10444. [CrossRef] [PubMed]
78. Sun, D.; Gao, Y.; Zhou, Y.; Yang, M.; Hu, J.; Lu, T.; Wang, T. Enhance Fracture Toughness and Fatigue Resistance of Hydrogels by Reversible Alignment of Nanofibers. *ACS Appl. Mater. Interfaces* **2022**, *14*, 49389–49397. [CrossRef] [PubMed]
79. Wu, Y.; Zhang, Y.; Wu, H.; Wen, J.; Zhang, S.; Xing, W.; Zhang, H.; Xue, H.; Gao, J.; Mai, Y. Solvent-Exchange-Assisted Wet Annealing: A New Strategy for Superstrong, Tough, Stretchable, and Anti-Fatigue Hydrogels. *Adv. Mater.* **2023**, *35*, 2210624. [CrossRef] [PubMed]
80. Liang, X.; Chen, G.; Lin, S.; Zhang, J.; Wang, L.; Zhang, P.; Lan, Y.; Liu, J. Bioinspired 2D Isotropically Fatigue-Resistant Hydrogels. *Adv. Mater.* **2022**, *34*, 2107106. [CrossRef] [PubMed]
81. Fang, Y.; Li, J.; Bai, Z.; Wei, J.; Yang, K.; Yang, L.; Wang, Q.; Cui, J. Key roles of Young's modulus and mechanical hysteresis in hydrogel strain sensors for high-fidelity sensing. *Sci. China Mater.* **2026**, *69*, 1624–1633. [CrossRef]
82. Lu, J.; Zhao, Z.; Liao, X.; Liu, J.; Chen, J.; Li, Y.; Wang, Y.; Zhang, Y.; Li, J.; Li, T.; et al. Topologically entangled zwitterionic hydrogels with reversible in situ transitions between ultraplastic and hyperelastic states. *Nat. Commun.* **2026**, *17*, 6527. [CrossRef] [PubMed]
83. Si, M.; Tang, Y.; Xu, C.; Li, C.Y.; Xia, K.; Xu, W.; Lin, J.; Jiang, Z.; Yang, J.; Zheng, S.Y. Developing tough, fatigue-resistant and conductive hydrogels via in situ growth of metal dendrites. *Mater. Horiz.* **2025**, *12*, 1452–1462. [CrossRef] [PubMed]
84. Huang, W.; Wang, X.; Luo, F.; Zhao, X.; Chen, K.; Qin, Y. Ultrastretchable, Ultralow Hysteresis, High-Toughness Hydrogel Strain Sensor for Pressure Recognition with Deep Learning. *ACS Appl. Mater. Interfaces* **2024**, *16*, 49834–49844. [CrossRef] [PubMed]
85. Cao, C.; Huang, T.; Li, Y. Resilient and Tough Conductive Polymer Hydrogel for a Low-Hysteresis Strain Sensor. *Macromol. Rapid Commun.* **2024**, *45*, 2300467. [CrossRef] [PubMed]
86. Prameswati, A.; Entifar, S.A.N.; Han, J.W.; Wibowo, A.F.; Kim, J.H.; Sembiring, Y.S.B.; Park, J.; Lee, J.; Lee, A.-Y.; Song, M.H.; et al. Self-Healable Conductive Hydrogels with High Stretchability and Ultralow Hysteresis for Soft Electronics. *ACS Appl. Mater. Interfaces* **2023**, *15*, 24648–24657. [CrossRef] [PubMed]
87. Wang, W.; Guo, P.; Liu, X.; Chen, M.; Li, J.; Hu, Z.; Li, G.; Chang, Q.; Shi, K.; Wang, X.; et al. Fully Polymeric Conductive Hydrogels with Low Hysteresis and High Toughness as Multi-Responsive and Self-Powered Wearable Sensors. *Adv. Funct. Mater.* **2024**, *34*, 2316346. [CrossRef]
88. Xu, L.; Liu, S.; Zhu, L.; Liu, Y.; Li, N.; Shi, X.; Jiao, T.; Qin, Z. Hydroxypropyl methyl cellulose reinforced conducting polymer hydrogels with ultra-stretchability and low hysteresis as highly sensitive strain sensors for wearable health monitoring. *Int. J. Biol. Macromol.* **2023**, *236*, 123956. [CrossRef] [PubMed]
89. Wu, P.; Tang, R.; Wu, S.; Li, W.; Jiang, Q.; Xiao, J.; Zhu, R.; Yan, Y. High-Strength, Low-Hysteresis Hydrogel Fibers via Coordination-Locked Entangled Networks for Wearable Sensors. *Small Methods* **2026**, e70876. [CrossRef] [PubMed]
90. Zhao, K.; Wang, J.; Wu, Y.; Yu, X.; Cao, H.; Yang, X.; Ni, A.; Ge, Y.; Liu, Y.; Zhuang, S.; et al. Silk fibroin-based hydrogels with low hysteresis, self-adhesion, and tunable ionic conductivity for wearable devices. *Int. J. Biol. Macromol.* **2025**, *306*, 141597. [CrossRef] [PubMed]
91. Wang, Y.; Song, L.; Wang, Q.; Wang, L.; Li, S.; Du, H.; Wang, C.; Wang, Y.; Xue, P.; Nie, W.-C.; et al. Multifunctional acetylated distarch phosphate based conducting hydrogel with high stretchability, ultralow hysteresis and fast response for wearable strain sensors. *Carbohydr. Polym.* **2023**, *318*, 121106. [CrossRef] [PubMed]
92. Liu, J.; Chen, X.; Sun, B.; Guo, H.; Guo, Y.; Zhang, S.; Tao, R.; Yang, Q.; Tang, J. Stretchable strain sensor of composite hydrogels with high fatigue resistance and low hysteresis. *J. Mater. Chem. A Mater.* **2022**, *10*, 25564–25574. [CrossRef]

93. Zhang, L.-Y.; Li, G.; Li, G.-N.; Hou, Y.-Z.; Li, H.; Xue, Y.; Zhao, W.-J.; Lu, B.-Y. Hysteresis-free and Fatigue-resistant Conductive Hydrogel Electronics towards Intelligent Human-machine Interaction. *Chin. J. Polym. Sci.* **2026**, *44*, 1830–1842. [CrossRef]
94. Li, W.; Xu, W.; Yang, L.; Lin, W.; Chen, Y.; Li, L.; Chen, S.; Zheng, C.; Huang, J.; Cai, W.; et al. Multi-synergistic strategy for dual-sensing conductive hydrogels capable of simultaneous strain and temperature monitoring. *FlexMat* **2026**, *3*, 415–427. [CrossRef]
95. Liu, D.; Zhou, H.; Zhao, Y.; Huyan, C.; Wang, Z.; Torun, H.; Guo, Z.; Dai, S.; Bin Xu, B.; Chen, F. A Strand Entangled Supramolecular PANI/PAA Hydrogel Enabled Ultra-Stretchable Strain Sensor. *Small* **2022**, *18*, 2203258. [CrossRef] [PubMed]
96. Zhang, Y.; Chen, X. In Situ Nanophase-Engineered, Filler-Free Dynamic Hydrogels Enable Cycle-Stable and Drift-Resistant Wearable Strain Sensors. *ACS Appl. Eng. Mater.* **2026**, *4*, 2886–2894. [CrossRef]
97. Cao, J.; Zhang, Z.; Wang, L.; Lin, T.; Li, H.; Zhao, Q.; Wang, H.; Liu, X.; Yang, H.; Lu, B. An adhesive, highly stretchable and low-hysteresis alginate-based conductive hydrogel strain sensing system for motion capture. *Int. J. Biol. Macromol.* **2024**, *281*, 136581. [CrossRef] [PubMed]
98. Wei, C.; Wang, Y.; Liang, Y.; Wu, J.; Li, F.; Luo, Q.; Lu, Y.; Liu, C.; Zhang, R.; Lu, Z.; et al. Low-hysteresis and highly linear sensors based on environmentally stable, adhesive, and antibacterial hydrogels. *J. Mater. Chem. A Mater.* **2024**, *12*, 10392–10402. [CrossRef]
99. Luo, L.; Wu, Z.; Ding, Q.; Wang, H.; Luo, Y.; Yu, J.; Guo, H.; Tao, K.; Zhang, S.; Huo, F.; et al. In Situ Structural Densification of Hydrogel Network and Its Interface with Electrodes for High-Performance Multimodal Artificial Skin. *ACS Nano* **2024**, *18*, 15754–15768. [CrossRef] [PubMed]
100. Zhao, W.; Lin, Z.; Wang, X.; Wang, Z.; Sun, Z. Mechanically Interlocked Hydrogel–Elastomer Strain Sensor with Robust Interface and Enhanced Water—Retention Capacity. *Gels* **2022**, *8*, 625. [CrossRef] [PubMed]
101. He, J.; Huang, J.; Li, R.; Chen, Z.; Li, Z.; Zhou, R.; Wang, S.; Gao, W.; Guo, C.F.; Bao, R.; et al. Hysteresis-free and dynamically resilient strain sensor enabled by interfacial coordination. *Sci. Adv.* **2026**, *12*, eaea2450. [CrossRef] [PubMed]
102. Zheng, Y.; Wang, Y.; Nakajima, T.; Gong, J.P. Effect of Predamage on the Fracture Energy of Double-Network Hydrogels. *ACS Macro Lett.* **2024**, *13*, 130–137. [CrossRef] [PubMed]
103. Ji, D.; Kim, D.-Y.; Fan, Z.; Lee, C.-S.; Kim, J. Hysteresis-Free, Elastic, and Tough Hydrogel with Stretch-Rate Independence and High Stability in Physiological Conditions. *Small* **2024**, *20*, 2309217. [CrossRef] [PubMed]
104. Kim, D.-Y.; Ji, D.; Jung, S.-Y.; Fan, Z.; Kim, J.; Lee, C.-S. Bioinspired Mineralized, Mechanically Reinforced Elastic Hydrogel without Hysteresis and Deformation-Rate Dependence. *Nano Lett.* **2025**, *25*, 12832–12841. [CrossRef] [PubMed]
105. Li, M.; Pu, J.; Cao, Q.; Zhao, W.; Gao, Y.; Meng, T.; Chen, J.; Guan, C. Recent advances in hydrogel-based flexible strain sensors for harsh environment applications. *Chem. Sci.* **2024**, *15*, 17799–17822. [CrossRef] [PubMed]
106. Du, T.; Zhu, Z.; Chen, M.; Yan, X.; Li, Y. Functional Hydrogel Strain Sensors for Smart Electronic Devices: Strategies and Recent Progress. *ACS Appl. Electron. Mater.* **2024**, *6*, 5402–5428. [CrossRef]
107. Tang, J.; Chen, Y.; Li, K.; Bai, Y.; Guo, R.; Fukuda, K.; Someya, T.; Ito, Y.; Kawamoto, M. Ultra-low hysteresis, high-toughness, anti-swelling nanocomposite hydrogel derived from dynamic multiple noncovalent interactions for wearable strain sensing and underwater gait recognition. *Chem. Eng. J.* **2025**, *516*, 163845. [CrossRef]
108. Wang, L.; Chen, W.; Li, H.; Xu, X.; Zhang, Z.; Wu, L.; Xu, J.; Huang, Y.; Lu, B. Ultrasoft, anti-dehydrated, and highly stretchable carboxymethylcellulose-based organohydrogel strain sensors for non-invasive real-time plant growth monitoring. *Carbohydr. Polym.* **2025**, *364*, 123753. [CrossRef] [PubMed]
109. Guo, X.; Li, J.; Wang, J.; Huang, L.; Cheng, G.; Zhang, Q.; Zhu, H.; Zhang, M.; Zhu, S. Stretchable Hydrogels with Low Hysteresis and High Fracture Toughness for Flexible Electronics. *Macromol. Rapid Commun.* **2022**, *43*, 2100716. [CrossRef] [PubMed]
110. Zheng, Y.; Wang, X.; Gao, Y.; Lu, T. Fatigue Damage-Tolerant Hydrogel Engineered via Synergy of Kinetically Distinct Metal–Ligand Crosslinks. *ACS Appl. Mater. Interfaces* **2026**, *18*, 43099–43108. [CrossRef] [PubMed]
111. Li, W.; Wang, X.; Liu, Z.; Zou, X.; Shen, Z.; Liu, D.; Li, L.; Guo, Y.; Yan, F. Nanoconfined polymerization limits crack propagation in hysteresis-free gels. *Nat. Mater.* **2024**, *23*, 131–138. [CrossRef] [PubMed]
112. Zhong, D.; Wang, Z.; Xu, J.; Liu, J.; Xiao, R.; Qu, S.; Yang, W. A strategy for tough and fatigue-resistant hydrogels via loose cross-linking and dense dehydration-induced entanglements. *Nat. Commun.* **2024**, *15*, 5896. [CrossRef] [PubMed]
113. Zhang, Z.; Chen, G.; Xue, Y.; Duan, Q.; Liang, X.; Lin, T.; Wu, Z.; Tan, Y.; Zhao, Q.; Zheng, W.; et al. Fatigue-Resistant Conducting Polymer Hydrogels as Strain Sensor for Underwater Robotics. *Adv. Funct. Mater.* **2023**, *33*, 2305705. [CrossRef]
114. Jia, L.; Wu, S.; Yuan, R.; Xiang, T.; Zhou, S. Biomimetic Microstructured Antifatigue Fracture Hydrogel Sensor for Human Motion Detection with Enhanced Sensing Sensitivity. *ACS Appl. Mater. Interfaces* **2022**, *14*, 27371–27382. [CrossRef] [PubMed]
115. Wu, H.; Wu, Y.; Yan, J.; Xiao, W.; Wang, Y.; Zhang, H.; Huang, X.; Xue, H.; Wang, L.; Tang, L.; et al. Organogel assisted salting out for strong and anti-fatigue hydrogels as wearable strain sensors. *Chem. Eng. J.* **2024**, *488*, 150963. [CrossRef]
116. Yuan, X.; Yang, Z.; Wang, Y.; Ju, J.; Yao, X. Stress-Shield Enhanced Fatigue Resistance in Fabric-Hydrogel Composite Coatings. *ACS Appl. Mater. Interfaces* **2026**, *18*, 36036–36045. [CrossRef] [PubMed]

117. Zhang, Z.; Xiao, S.; Pan, X.; Zheng, R.; Zeng, S.; Lu, J.; Chen, J.; Wang, L. Tough, rapid self-recovery and responsive hydrogel strain sensor for intelligent home-based rehabilitation monitoring system. *Chem. Eng. J.* **2026**, *540*, 177110. [CrossRef]
118. Sheng, Y.; Li, Z.; Gao, D.; Niu, P.; Gao, X.; Huang, Y.; Li, C.; Qiu, J.; Zhang, R.; Sun, Y. A Stretchable Conductive Material with High Fatigue Resistance for Strain Sensors. *ACS Appl. Mater. Interfaces* **2024**, *16*, 63840–63850. [CrossRef] [PubMed]

**Disclaimer/Publisher's Note:** The statements, opinions and data contained in all publications are solely those of the individual author(s) and contributor(s) and not of MDPI and/or the editor(s). MDPI and/or the editor(s) disclaim responsibility for any injury to people or property resulting from any ideas, methods, instructions or products referred to in the content.